

**A Defective Thesis: Studying the Behaviour of Defects in
Liquid-Crystalline Materials**

by

A. A. S. Green

B.Sc., University of Calgary 2011

M.S., University of Colorado at Boulder 2015

A thesis submitted to the
Faculty of the Graduate School of the
University of Colorado in partial fulfillment
of the requirements for the degree of
Doctor of Philosophy
Department of Physics
2019

This thesis entitled:
A Defective Thesis: Studying the Behaviour of Defects in Liquid-Crystalline Materials
written by A. A. S. Green
has been approved for the Department of Physics

Prof. Noel Clark

Professor Leo Rhadzihofsky

Professor David Walba

Date _____

The final copy of this thesis has been examined by the signatories, and we find that both the content and the form meet acceptable presentation standards of scholarly work in the above mentioned discipline.

Green, A. A. S. (Ph.D., Physics)

A Defective Thesis: Studying the Behaviour of Defects in Liquid-Crystalline Materials

Thesis directed by Prof. Noel Clark

Dedication

To my parents.

Acknowledgements

Here's where you acknowledge folks who helped. But keep it short, i.e., no more than one page, as required by the Grad School Specifications.

Contents

Chapter

1	Introduction	1
1.1	Liquid Crystals	1
1.1.1	Phases of matter	1
1.1.2	The Rod Liquid Crystal	1
1.1.3	The Bent Liquid Crystal	1
1.1.4	Characterization of Liquid Crystals: Case Study	1
1.2	Fluid Dynamics	1
1.3	Fluid Dynamics of Liquid Crystals	1
2	The Discovery of Helicity in Tilted Bent-Core Smectics: $\text{Sm}(\text{CP})_\alpha$	2
2.1	Characterization of PAL30	3
2.1.1	Experimental Details	4
2.1.2	Differential Scanning Calorimetry of PAL30	5
2.1.3	X-ray Scattering of PAL30	7
2.1.4	Optical Textures	12
2.1.5	Polarization Current	16
2.2	Results and Discussion	19
3	chirality on demand: the study of a homologous series of molecules	21
3.0.1	Textures of bent-core de Vries phase	21

3.0.2	Electro-optics of bent-core de Vries phase	21
3.0.3	X-ray analysis of bent-core de Vries phase	21
3.1	Discussion for the bent-core de Vries phase	21
4	Metrology Applications of Fluid Crystals	25
4.1	Experimental Design	25
4.2	Theory and Simulation	28
4.3	Results and Discussion	32
Bibliography		35
Appendix		

Tables**Table**

Figures

Figure

2.1 Experimental characterization of PAL30. (a) The PAL30 molecule, showing the all-trans length calculated using the program Spartan. (b–d) Phase properties vs. temperature. The solid vertical lines denote phase boundaries and the cross-hatching phase coexistence. (b) SAXS shows the smectic layer spacing in all phases to be $d_0 \approx 48 \text{ \AA}$. Resonant carbon K-edge reflections are from superlayer modulations of the molecular orientation about the layer normal z , the peak at $d_H \approx 150 \text{ \AA}$ corresponding to the pitch of the incommensurate, helical precession in the Sm2 phase, and at $d_B = 2d_0$ to the bilayer ordering of the Sm3 and Sm4 phases. (c) Birefringence of planar-aligned cells with layers normal to the plates, with and without applied electric field ($E = 20 \text{ V}/\mu\text{m}$). (d) Polarization current (in nA) in response to a triangle-wave applied electric field: a single-peak, Langevin-like response at lower temperatures in the Sm1 phase; a triple peak in the Sm2 phase, associated with ferrielectric switching[10] and indicative of helical unwinding[43], coalescing into a double peak in the Sm3, indicating a non-polar ground state at $E = 0$; and a single current peak in the Sm4 phase caused by the block polarization switching of the ferroelectric Sm_{C_A}P_F ground state. (e–m) Characteristic optical textures in a planar cell, viewed between crossed polarizers. The $E = 0$ textures are focal conics typical of a fluid smectic with an optic axis along z . Field application induces chiral, tilted conglomerate domains (of opposite handedness) in the Sm1–Sm3 phases, but only a change in birefringence in the Sm4. (n–q) Proposed superlayer structure of PAL30 phases, with and without applied electric field: (n) Sm1: achiral de Vries-like SmA → chiral Sm_{C_S}P_F; Sm2: superlayer chiral helix → chiral Sm_{C_S}P_F; Sm3: superlayer chiral bilayer Sm_{C_A}P_A → chiral Sm_{C_S}P_F; Sm4: Sm_{C_A}P_F with \mathbf{P} parallel to the glass → Sm_{C_A}P_F with \mathbf{P} normal to the glass.

2.2	Differential scanning calorimetry of PAL30. On cooling, there is only a small, enthalpy peak at $\approx 110^\circ\text{C}$ corresponding to the transition from the highest-temperature smectic phase, the Sm1, and the Sm2.	7
2.3	X-ray scattering of high temperature phase, Sm1, of $\text{Sm}(\text{CP})_\alpha$. (a) The smectic layer size, d , increases monotonically on cooling, with no inflection points that would be characteristic of a untilted \rightarrow tilted phase transition. (b) No resonant scattering is observed for this phase.	8
2.4	Temperature behaviour of the $\text{Sm}(\text{CP})_\alpha$ phase plotted as a waterfall plot in (a), and as a contour plot in (b). A bilayer ($d = 112 \text{ \AA} = 2d_0$) corresponds to the 2-layer unit-cell structure of the $\text{SmC}_\text{A}P_\text{A}$ phase, which sits directly below the $\text{Sm}(\text{CP})_\alpha$ phase in temperature. The resonant peak corresponding to the $\text{Sm}(\text{CP})_\alpha$ phase at $d \approx 150 \text{ \AA}$ is direct evidence that the $\text{Sm}(\text{CP})_\alpha$ phase is not a classic B2-type phase.	9
2.5	X-ray scattering from PAL30. (a) SAXS gives a peak from the smectic layer ordering at $q = q_0$. The RSoXS peak at q_H indicates that there is superlayer orientational ordering with periodicity d_H in the Sm2 phase. In general, superlayer orientational modulation in a smectic generates RSoXS peaks at wavevectors along the layer normal at $q(l, m) = l(2\pi/d_0) \pm m(2\pi/d_H)$ [19]. The observation of an RSoXS reflection at $q = q(0, 1)$ and the absence of an Umklapp peak at $q = q(1, -1)$ in the Sm2 confirms a superlayer helix with a scattering amplitude modulation due to the smectic layering that is undetectably weak. (b) Temperature dependence of resonant scattering. The helix peak at $q_H \approx 1/(2.8d_0)$ becomes diffuse in the Sm3 phase. Splitting of the bilayer peak at q_B , which would indicate helical precession of the bilayer structure, is not observed.	11
2.6	Planar aligned textures of Sm1. (a) Applied field out of the page, (b) ground state (no field), (c) applied field into the page.	12

2.7 Optical tilt of PAL30 vs. applied field. The Sm1 phase shows no electrooptic response in weak fields $E < E_{\text{th}}$. Fields $E > E_{\text{th}}$ induce an electroclinic tilt and result in the formation of chiral domains. E_{th} , which becomes smaller with decreasing T (inset), matches closely E_{sat} , the field at which the induced polarization saturates, extracted from Figure 2.1(d). The Sm2 phase exhibits a chiral electroclinic effect near $E = 0$ and hysteresis in the field-induced helix unwinding to the $\text{SmC}_S P_F$ state.	13
2.8 Calculated birefringence of PAL30, assuming Boulder phase assignments, shown as a function of temperature	14
2.9 Textures of both the Sm2 ($\text{Sm}(\text{CP})_\alpha$) and Sm3 ($\text{SmC}_A P_A$) phases of PAL30: reminiscent of a $\text{SmC}_A P_A$ texture.	15
2.10 Textures of both the Sm2 ($\text{Sm}(\text{CP})_\alpha$) and Sm3 ($\text{SmC}_A P_A$) phases of PAL30: reminiscent of a $\text{SmC}_A P_A$ texture.	15
2.11 Polarization current of PAL30 shown as a function of the applied field strength.	16
2.12 Zoomed in polarization current measurements for PAL30 in the high temperature Sm1 phase.	17
2.13 The polarization current and the optical tilt plotted as a function of applied field strength for both the Sm1 (de Vries SmA) (a,b) and the Sm2 ($\text{Sm}(\text{CP})_\alpha$) (c-d). The polarization current has additionally been integrated to calculate the time-dependant net polarization. The threshold electric field (E_{th}) required to manifest the tiger-stripes can be directly read from the green curve denoting the optical tilt (for $T=110^\circ\text{C}$, $E_{\text{th}} \approx 5 \text{ V}/\mu\text{m}$), and the saturation electric field where the net polarization is no longer changing (E_{sat}) can be directly read from the red curve, which denotes the net polarization, (for $T=110^\circ\text{C}$, $E_{\text{sat}} \approx 5 \text{ V}/\mu\text{m}$). Both E_{th} and E_{sat} are plotted in as the inset of Figure 2.7.	17
2.14 Polarization current of sm2 of PAL30 plotted against applied voltage	18

2.15	Polarization current measurements for PAL30 in the high temperature SmI phase.	19
2.16	Evolution of de Vries SmA bent-core phase under the application of a field	20
3.1		21
3.2		22
3.3		22
3.4		23
3.5		23
3.6		24
4.1	Smectic film flow meter geometry. (a) A stainless steel film holder (45.2 mm × 34.8 mm × 7.6 mm) has a $w = 3.1$ mm-wide channel in the form of a racetrack cut to a depth $h = 3.7$ mm. At viewing ports centered along each ‘arm’, the channel is cut all the way through the film holder (a depth of 7.6 mm). Gas is coupled into and out of the system by means of co-linear, 2 mm-diameter holes at the ends of the film holder. Smectic films are created by coating the bottom of a glass coverslip (the spreader) with liquid crystal material and drawing it across the top opening of the channel. The film is shielded from random air currents from above by a sealed cover (not shown). The photomicrograph shows typical islands (localized regions with more layers than the background film) used to track flow of the film in one of the viewing regions of the racetrack. (b) Schematic cross-section of a smectic film suspended across the channel (not to scale). The film comprises an integer number of smectic layers and can be as thin as two molecules (~ 6 nm). In general, a meniscus forms where the film contacts the edges of the channel.	26

- 4.2 Analytic analysis of symmetric, two-phase, stratified fluid flow in an infinitely long pipe of width a . (a) Ratio between the average film and air velocities as a function of the phase fraction (the ratio of the volume of the fluid and the volume of the air, $\phi = h_{\text{film}}/h_{\text{air}}$). When the phase fraction is very small, the film is strongly coupled to the air and moves with the same speed. (b) Flow velocity in the top half of the pipe. At left, both air and film are flowing through the pipe (the blue dashed line demarcates the upper boundary of the film), while on the right only air is present. The y dimension is scaled by the half the thickness of the LC film, h_{film} . The flow fields in these two cases are practically indistinguishable, suggesting that the influence of the LC film on the airflow is negligible. 29
- 4.3 Computed airflow in the racetrack geometry. (a) Model velocity field for inlet velocity $v_{\text{inlet}} = 0.15 \text{ m/s}$. The air does not circulate uniformly in the same sense around the racetrack, instead splitting between the front and back legs. (b) Model velocity field for inlet velocity $v_{\text{inlet}} = 0.65 \text{ m/s}$. Above a transition inlet velocity of $v_{\text{inlet}} = 0.55 \text{ m/s}$, the air circulates uniformly around the racetrack. (c) Predicted net film speed ($v_{\text{film}} \propto v_2 - v_1$) for a range of inlet velocities. The slope of this curve gives an average theoretical sensitivity of $S = 0.15$. The background shading reflects the experimental observations with different inlet velocities: for $v_{\text{in}} < 0.3 \text{ m/s}$, the film flow is chaotic; for $0.3 \text{ m/s} < v_{\text{in}} < 1.2 \text{ m/s}$, the film exhibits stable Poiseuille flow; for $v_{\text{in}} > 1.2 \text{ m/s}$, the film undergoes rapid out-of-plane oscillations that make particle tracking impractical. 31

- 4.4 Characterization of flow meter. (a) Velocity profiles over the width of the racetrack channel, with each point corresponding to a specific tracked island. The profiles are well described by parabolas (smooth curves), confirming Poiseuille flow over a wide-range of inlet velocities. At higher velocities, the data are noisier due to the relatively paucity of islands that can be captured in sequential frames. The left-right asymmetry in the number of measurements is an artifact due to defects on one side of the camera sensor. (b) Spatially averaged film velocity in the observation region as a function of inlet air velocity. Measurements were performed over four separate days, using more than 30 films. The volumetric flow rate of the air being injected into the racetrack through the inlet was measured using an independent mechanical sensor. The average film speed is linearly proportional to the speed of the air at the device inlet, with a sensitivity that is independent of flow rate.

Chapter 1

Introduction

1.1 Liquid Crystals

1.1.1 Phases of matter

1.1.2 The Rod Liquid Crystal

1.1.3 The Bent Liquid Crystal

1.1.4 Characterization of Liquid Crystals: Case Study

1.2 Fluid Dynamics

1.3 Fluid Dynamics of Liquid Crystals

Chapter 2

The Discovery of Helicity in Tilted Bent-Core Smectics: $\text{Sm}(\text{CP})_\alpha$

The discovery of spontaneous macroscopic polar ordering [25] and chirality [21] in fluid smectic liquid crystal phases of achiral bent-core mesogens has led to the exploration of a rich family of novel liquid crystal phases and self-assemblies [41, 8, 42, 6, 33] in which the key macroscopic elements of polarity, chirality, and smectic layering all appear as spontaneously broken symmetries. While the smectic layer-scale order of bent-core mesogens, resulting from strong intralayer coupling between molecular tilt and polarity, is quite well characterized, superlayer structuring beyond that of the four basic SmCP bilayer phases combining synclinic or anticlinic tilt with ferroelectric or antiferroelectric polarity [21], as sketched in Supplemental Figure S1, have not been definitively identified. Possible superlayer structures analogous to those seen in tilted SmC^* phases of chiral, rod-shaped molecules could be incommensurate or commensurate with the underlying smectic layer spacing and feature states of varying azimuthal orientation of the molecular long axis about the layer normal, z , such as the chiral helical precession along z with equal, discrete orientational jumps between layers of the SmC_α^* phase and the ferrielectric phases with periodic arrays of discrete jumps of different sizes [43].

Since the period of such superlayer structures, p , can be as short as two layers, the structural study of such phases requires the effective probing of molecular orientation at the nanoscale. This can be achieved using resonant X-ray scattering, a technique sensitive to

put
joe
prc in
begin-
ning
of sub-
sec-
tion

put
biref/tilt
figure
in the
optical
textures/ele
optics
sec-
tion

atomic environment [24, 19, 23, 14, 12, 5, 11, 15, 50, 49, 36] that has previously enabled the discovery and definitive characterization of superlayer organization in several SmC* phases and sub-phases, employing the K-edge resonance of atoms incorporated in the liquid crystal molecule [24, 23].

Several recent observations suggest the possibility of chiral superlayer ordering in achiral bent-core mesogens: Takanishi et al. have identified such a structure in a SmCP phase of a bent-core mesogen doped with a chiral, rod-shaped molecule that as a neat material exhibits SmC $_{\alpha}^*$ and ferrielectric phases [40]; Abberley et al. have reported a superlayer helix in a smectic phase of bent dimers of molecular rods [1]; Panarin and co-workers have recently proposed, based on AFM evidence, the existence of tilted, helical supermolecular ordering in several achiral bent-core mesogens with 4-cyanoresorcinol bisbenzoate cores [39]. Earlier investigations of this molecular family had concluded, however, that their polar phases were orthogonal, i.e., untilted and therefore not chiral [26, 38]. Motivated by these conflicting reports and the ongoing interest in the chiral sub-phases of liquid crystals, we have studied one of the members of this homologous series, PAL30, which has $n = 14$ alkyl tails (see Figure 2.1(a)). Our experiments, using non-resonant X-ray scattering (SAXS), resonant soft X-ray scattering (RSoXS), electro-optic techniques, and polarized light microscopy (PLM), summarized in Figure 2.1, reveal an exotic phase sequence, including an achiral de Vries smectic which becomes chiral in sufficiently large applied electric fields, and, at lower temperature, a tilted, chiral smectic with superlayer helical ordering.

2.1 Characterization of PAL30

We used a combination of two-dimensional, small-angle, hard X-ray scattering (SAXS), resonant, soft X-ray scattering (RSoXS), differential scanning calorimetry (DSC), polarized, transmitted light microscopy on cells in transmission, and measurements of the polarization reversal current of cells in order to characterize PAL30. These experiments reveal four smectic

phases, labeled in order of descending temperature as Sm1, Sm2, Sm3, and Sm4.

2.1.1 Experimental Details

The RSoXS experiments were performed at the Advanced Light Source at Lawrence Berkeley National Laboratory beamline 11.0.1.2 using linearly polarized X-ray photons [44, 22]. The X-ray energy was tuned between 270 eV and 290 eV in our experiments, with scattering contrast appearing only for energies near the carbon K-edge resonance ($E = 284$ eV), indicating the presence of real-space features with an orientational modulation. The PAL30 material was sandwiched between two silicon nitride substrates, while in the isotropic phase. The cell was then placed into a temperature controlled hotstage in the beamline. After finding the highest temperature where scattering features were observed, the sample was cooled slowly while recording 2D diffractograms of the scattering. The RSoXS setup is sensitive to orientational modulations from $d = 50$ Å to 1250 Å. The relative positions and orientations of the sample and detector were calibrated using a sample with known scattering q -values. The data from the detector was processed using the Igor Pro-based NIKA data reduction software package [17, 48].

The angular resolution of the diffractometer, estimated from the full width at half-maximum of a resonant feature known to be twice the smectic layer spacing is $\delta q \sim 0.00078$ Å⁻¹.

SAXS measurements were carried out on beamline X10A of the National Synchrotron Light Source (NSLS), at Brookhaven National Laboratory. This beamline has a Si 111 double monochromator, tuned to around 10 keV. The sample was mounted in an Instec hot stage on a Huber four-circle goniometer. The angular resolution of the diffractometer, measured by scanning the detector arm through the attenuated direct beam, is $\delta q \sim 0.005$ nm⁻¹ full width at half-maximum.

The planar cells used for texture analysis were 4.5 μm thick commercial cells purchased

from Instec Inc. with rubbed polyimide planar alignment layers and ITO glass. The thickness of the empty cells was measured using a visible light spectrometer. The cells were then filled with PAL30 in the isotropic phase. Polarization reversal current was measured in these cells by applying an alternating, triangular voltage.

The birefringence was measured using a Zeiss quartz-wedge compensator and a 5.86 μm thick Instec cell.

The molecular length of PAL30 was estimated using a Hartree-Fock 6-31G* calculation of a single molecule in the gas phase using the Spartan $\text{\AA}^{\circ}16$ numerical calculation package.

2.1.2 Differential Scanning Calorimetry of PAL30

The DSC reveals only a single enthalpy peak on cooling, at approximately 110 $^{\circ}\text{C}$, hinting that the Sm1 \rightarrow Sm2 transition is either a weakly first order, or a second order transition.

The lack of other enthalpy peaks is concerning, considering we identify four unique smectic phases in the phase sequence of PAL30. However, the resonant scattering experiments described in subsection 2.1.3, particularly the soft-melting mode seen in Figures 2.4, shows that the phase transition from the Sm2 \rightarrow Sm3 is strongly second order, spanning a temperature range of 10 $^{\circ}\text{C}$, which explains the absence of a distinct enthalpy peak in the DSC for this transition

The lack of a distinct peak for the Sm3 \rightarrow Sm4 peak has two plausible explanations. First, the polarization current shown in ?? shows that the transition is likely second order, spanning a temperature range of approximately 5 $^{\circ}\text{C}$, like the Sm2 \rightarrow Sm3. Though, as the identified structures of the Sm3 ($\text{SmC}_\text{A}P_\text{A}$) and Sm4 ($\text{SmC}_\text{A}P_\text{F}$) cannot be connected by a continuous deformation the same way the helical Sm2 (Sm(CP)_α) can be deformed into the Sm2 ($\text{SmC}_\text{A}P_\text{A}$), this seems less likely.

The other explanation, which I consider more likely, is due to the fact the DSC is

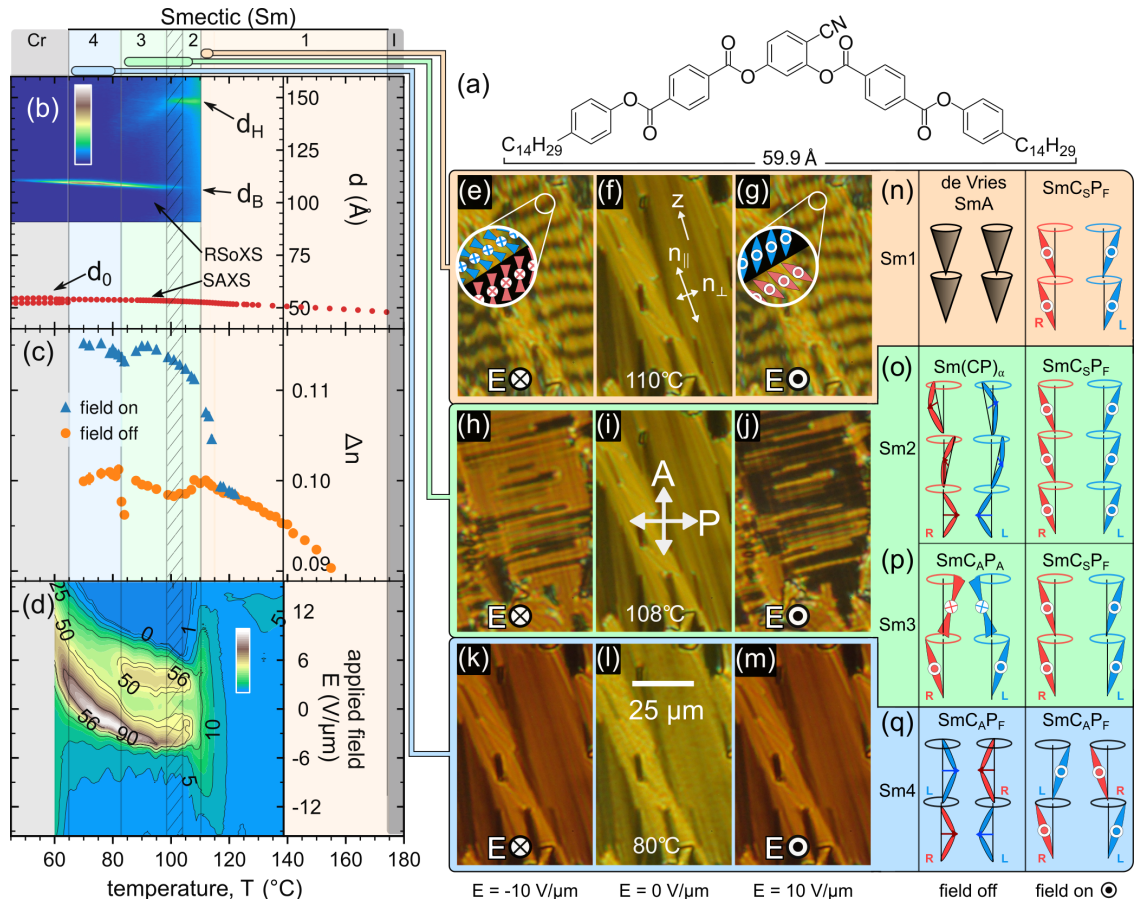


Figure 2.1: Experimental characterization of PAL30. (a) The PAL30 molecule, showing the all-trans length calculated using the program Spartan. (b–d) Phase properties vs. temperature. The solid vertical lines denote phase boundaries and the cross-hatching phase coexistence. (b) SAXS shows the smectic layer spacing in all phases to be $d_0 \approx 48 \text{ \AA}$. Resonant carbon K-edge reflections are from superlayer modulations of the molecular orientation about the layer normal z , the peak at $d_H \approx 150 \text{ \AA}$ corresponding to the pitch of the incommensurate, helical precession in the Sm2 phase, and at $d_B = 2d_0$ to the bilayer ordering of the Sm3 and Sm4 phases. (c) Birefringence of planar-aligned cells with layers normal to the plates, with and without applied electric field ($E = 20 \text{ V}/\mu\text{m}$). (d) Polarization current (in nA) in response to a triangle-wave applied electric field: a single-peak, Langevin-like response at lower temperatures in the Sm1 phase; a triple peak in the Sm2 phase, associated with ferrielectric switching[10] and indicative of helical unwinding[43], coalescing into a double peak in the Sm3, indicating a non-polar ground state at $E = 0$; and a single current peak in the Sm4 phase caused by the block polarization switching of the ferroelectric Sm_{CA}P_F ground state. (e–m) Characteristic optical textures in a planar cell, viewed between crossed polarizers. The $E = 0$ textures are focal conics typical of a fluid smectic with an optic axis along z . Field application induces chiral, tilted conglomerate domains (of opposite handedness) in the Sm1–Sm3 phases, but only a change in birefringence in the Sm4. (n–q) Proposed superlayer structure of PAL30 phases, with and without applied electric field: (n) Sm1: achiral de Vries-like SmA → chiral Sm_{Cs}P_F; Sm2: superlayer chiral helix → chiral Sm_{Cs}P_F; Sm3: superlayer chiral bilayer Sm_{CA}P_A → chiral Sm_{Cs}P_F; Sm4: Sm_{CA}P_F with **P** parallel to the glass → Sm_{CA}P_F with **P** normal to the glass.

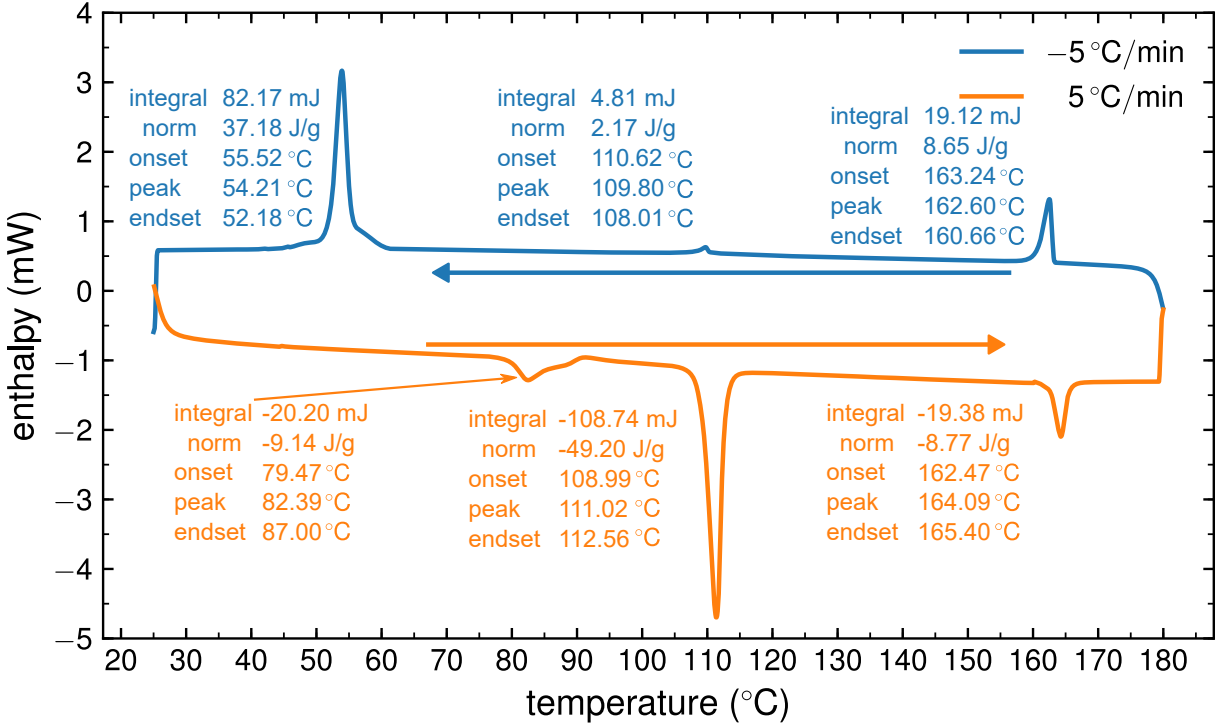


Figure 2.2: Differential scanning calorimetry of PAL30. On cooling, there is only a small, enthalpy peak at $\approx 110^\circ\text{C}$ corresponding to the transition from the highest-temperature smectic phase, the Sm1, and the Sm2.

measured without a field present, raising the possibility first explored by Guzman[?] for orthogonal phases, that the transition from the $\text{SmC}_\text{A}P_\text{A}$ to the $\text{SmC}_\text{A}P_\text{F}$ could be a kinetic trap. If this was the case, then the $\text{SmC}_\text{A}P_\text{A}$ would be expected to be the ground-state phase *in absence of an applied field* for the remainder of the phase sequence. This could be tested in future experiments with the DC hysteresis measurements described in Dr. Guzman's thesis[?].

2.1.3 X-ray Scattering of PAL30

X-ray scattering from PAL30 is shown in Figures 2.1(b) and S3.

Upon cooling from the isotropic, a single, non-resonant SAXS peak appears at 175°C ,

at a wavevector q_0 corresponding to Bragg scattering from the smectic layers in the Sm1 phase with spacing $d_0 = 2\pi/q_0 = 48 \text{ \AA}$.

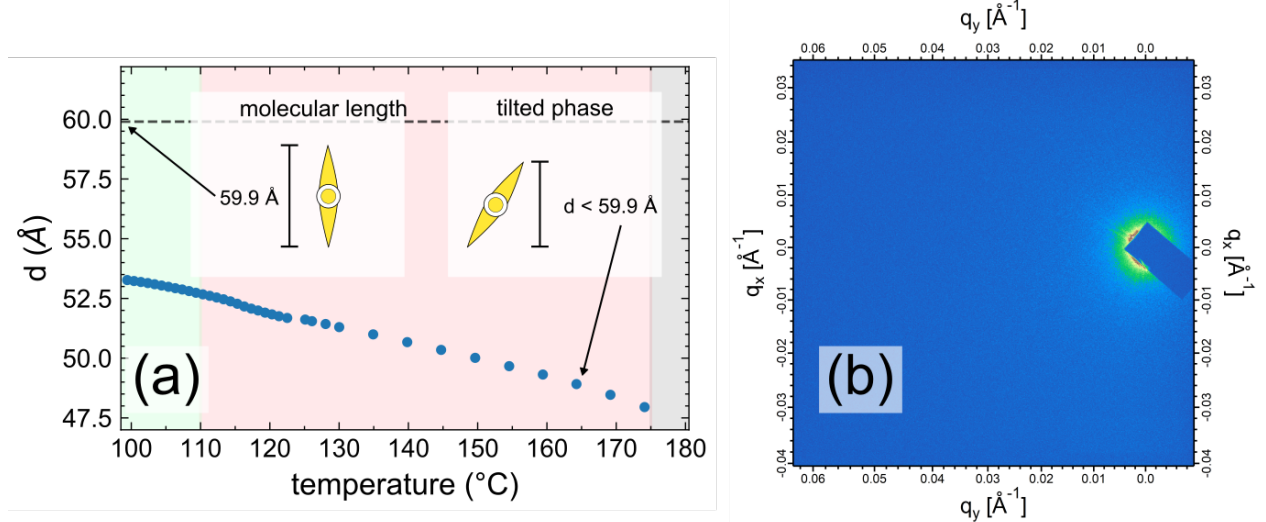


Figure 2.3: X-ray scattering of high temperature phase, Sm1, of $\text{Sm}(\text{CP})_\alpha$. (a) The smectic layer size, d , increases monotonically on cooling, with no inflection points that would be characteristic of a untilted \rightarrow tilted phase transition. (b) No resonant scattering is observed for this phase.

The layer spacing increases slightly on cooling to the crystal phase at 65°C and is consistently smaller than the calculated molecular length, $l = 59.9 \text{ \AA}$, throughout this temperature range, suggesting that the molecules are tilted in all of the smectic phases, to first order by an average amount estimated using $\theta_{\text{xray}} = \cos(d_0/l)$ of 33° (see Figure S4). In the Sm1 temperature range ($110^\circ\text{C} \leq T \leq 175^\circ\text{C}$), there are no RSoXS scattering features (Figure 2.3 (b)) that would indicate a superlayer periodic structure.

At the transition to the Sm2 phase, at 110°C , marked by a distinct enthalpy peak in the DSC (Figure S5), a single, sharp resonant peak appears at $q_H = 0.042 \text{ \AA}^{-1}$, corresponding to a molecular orientational structure with a period $d_H = 148 \text{ \AA} \approx 2.8d_0$ that is incommensurate with the smectic layer spacing (Figure 2.5(b) and Figure 2.4). Below 104°C , this reflection becomes weaker and another sharp, resonant reflection at higher q grows in, the coexistence indicating a first-order transition to the Sm3 phase. This second Bragg peak, which persists

down to the crystal phase, has a wavevector $q_B \approx q_0/2$, indicative of a commensurate, bilayer orientational structure in the Sm3 and Sm4 phases.

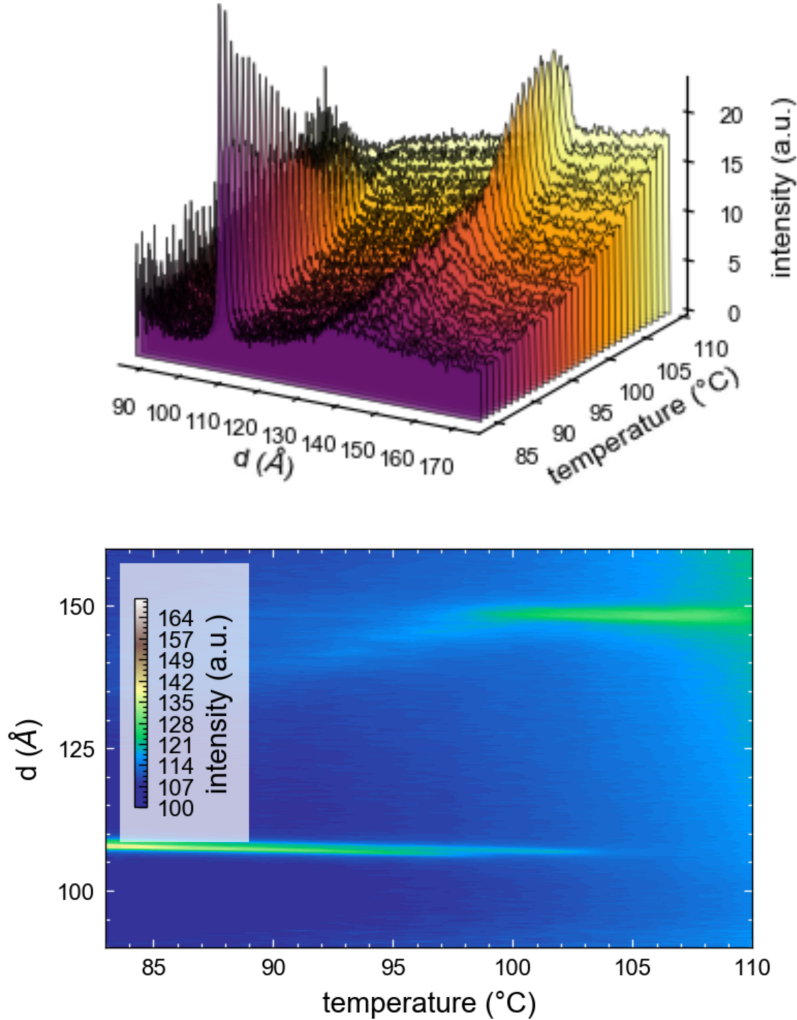


Figure 2.4: Temperature behaviour of the $\text{Sm}(\text{CP})_\alpha$ phase plotted as a waterfall plot in (a), and as a contour plot in (b). A bilayer ($d = 112 \text{ \AA} = 2d_0$) corresponds to the 2-layer unit-cell structure of the SmCPA phase, which sits directly below the $\text{Sm}(\text{CP})_\alpha$ phase in temperature. The resonant peak corresponding to the $\text{Sm}(\text{CP})_\alpha$ phase at $d \approx 150 \text{ \AA}$ is direct evidence that the $\text{Sm}(\text{CP})_\alpha$ phase is not a classic B2-type phase.

Below 99°C , the incommensurate peak broadens dramatically and moves to higher q , indicating the presence of short-ranged, Sm2-like helical fluctuations persisting in the Sm3

phase, and disappears at the transition to the Sm4 phase at 83 °C. The Sm4 phase exhibits only the bilayer RSoXS reflection at q_B .

The RSoXS scattering from a single layer can be analyzed, following Levelut and Pansu, in terms of a monoclinic second-rank tensor with a principal axis tilted from and then azimuthally rotated about the layer normal [19, 12, 5]. Scattering from a stack of such layers is calculated by summing over the contributions of the individual layers at different z . Resonant scattering peaks from azimuthally periodic arrangements are found at wavevectors along z , $q(l, m) = l(2\pi/d_0) \pm m(2\pi/p)$, where p is the pitch. In principle, resonant scattering should appear at all values of l (harmonics of q_0), and at values of $m = 0, \pm 1, \pm 2$ that depend on the superlayer structure. In an incommensurate, helical structure, like the SmC α phase, only the fundamental and harmonic peaks at $q(l = 0, m = +1, +2)$ and the Umklapp peaks at $q(l = +1, m = -1, -2)$ are found in the range $0 < q(l, m) < q_0$. If the resonant scatterers are confined to lie precisely on layers spaced by d_0 , then the intensities of these peaks will be identical [19]. Out-of-layer molecular positional fluctuations, and, in particular, those for which there is a coupled azimuthal orientation that keeps the molecule on the helix, $\delta\phi = (2\pi/p)\delta z$, reduce the intensities of the resonant harmonic peak at $2q_H$ and of the Umklapp peaks at $q_0 \pm q_H$, relative to that of the fundamental at q_H [19]. In our RSoXS scans of these peaks, only the fundamental is seen above the background, so that only the upper limit of the intensity ratio of the Umklapp and fundamental peaks can be estimated. From the RSoXS heating scan of Figure 2.5(a), we find $I_U/I_F \lesssim 0.03$, implying a very weak fractional modulation of the density of helical scatterers, ρ , due to fluctuations in the smectic layering $\sqrt{\langle \delta\rho^2 \rangle}/\rho_0 < 0.17$. The absence of the harmonic peaks places a similar limit on how much the density modulation of helical scatterers deviates from being purely sinusoidal.

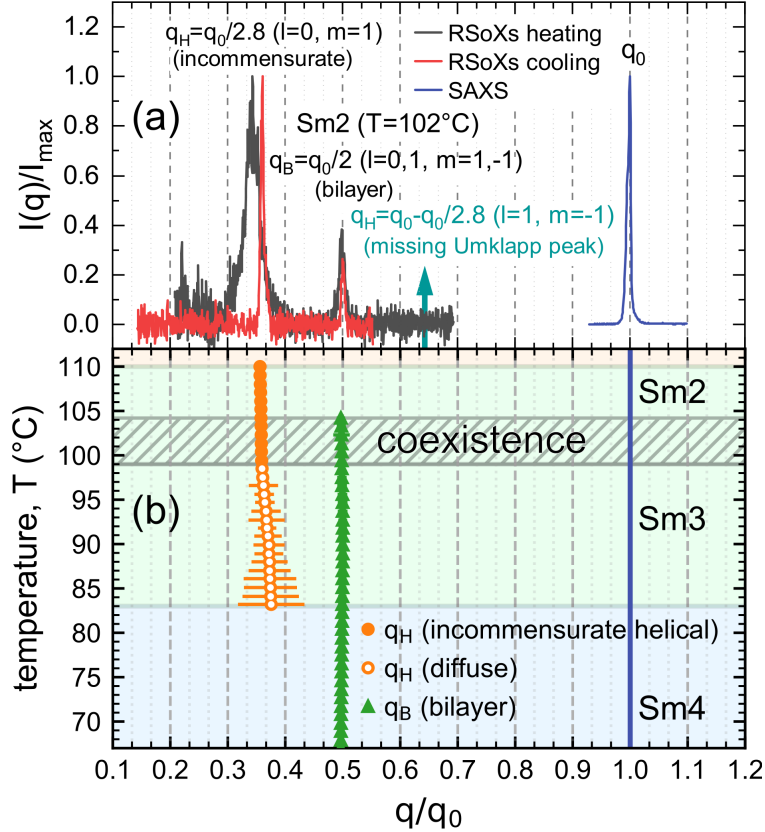


Figure 2.5: X-ray scattering from PAL30. (a) SAXS gives a peak from the smectic layer ordering at $q = q_0$. The RSoXS peak at q_H indicates that there is superlayer orientational ordering with periodicity d_H in the Sm2 phase. In general, superlayer orientational modulation in a smectic generates RSoXS peaks at wavevectors along the layer normal at $q(l, m) = l(2\pi/d_0) \pm m(2\pi/d_H)$ [19]. The observation of an RSoXS reflection at $q = q(0, 1)$ and the absence of an Umklapp peak at $q = q(1, -1)$ in the Sm2 confirms a superlayer helix with a scattering amplitude modulation due to the smectic layering that is undetectably weak. (b) Temperature dependence of resonant scattering. The helix peak at $q_H \approx 1/(2.8d_0)$ becomes diffuse in the Sm3 phase. Splitting of the bilayer peak at q_B , which would indicate helical precession of the bilayer structure, is not observed.

2.1.4 Optical Textures

The optical textures of planar-aligned (bookshelf) cells of PAL30 were studied using PLM. Upon cooling from the isotropic, the Sm1 phase grows in (at 175 °C) as bâtonnets, giving a smooth, focal-conic texture typical of an orthogonal fluid smectic (Figure 2.1(f), Figure 2.6).

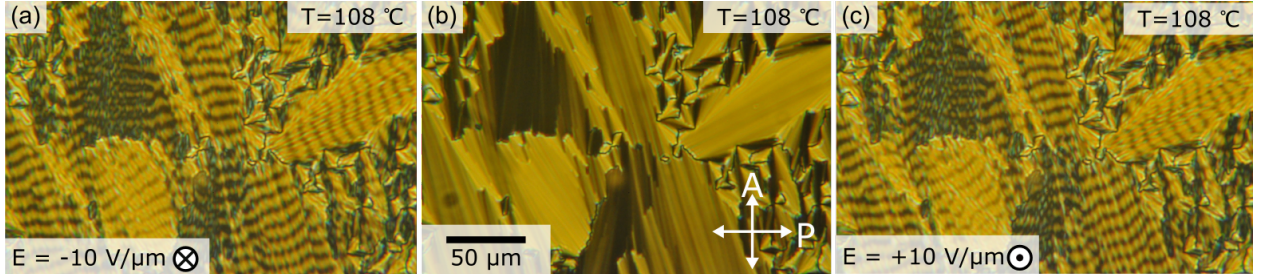


Figure 2.6: Planar aligned textures of Sm1. (a) Applied field out of the page, (b) ground state (no field), (c) applied field into the page.

However, given the large value of the estimated molecular tilt, θ_{xray} , the Sm1 is probably a de Vries smectic. In planar-aligned cells, there is no observable field-induced change of the in-plane birefringence, $\Delta n = n_{\parallel} - n_{\perp}$, in small applied electric fields (Figure 2.1(f)), or in the optic axis orientation, θ_{opt} (Figure 2.7).

Below 115 °C, a threshold field, E_{th} , above which a first-order structural change marked by the appearance of chiral conglomerate domains occurs, becomes experimentally accessible. These domains are polar and exhibit a uniform, saturated optic axis tilt on the order of $\theta_{\text{opt}} \approx 18^\circ$ from the layer normal, implying that the achiral, untilted Sm1 phase transforms in the field to a B2-like, homochiral $\text{SmC}_S P_F$ state (Figure S1(c)) [9]. The field-induced left- and right-handed domains form a “tiger stripe” pattern (Figures 2.1(e,g)).

The local domain handedness in this unusual conglomerate texture is apparently locked in after the first few field cycles. This bias is due to a chiral memory effect at the surface since, as Figures 2.1(d) and 2.7 show, the sub-threshold bulk state has an achiral field response, with

a linear polarization current (implying $P \propto E$) and no detectable reorientation of the optical tilt. E_{th} decreases strongly on cooling as the transition to the Sm2 phase is approached, as shown in the inset of Figure 2.7.

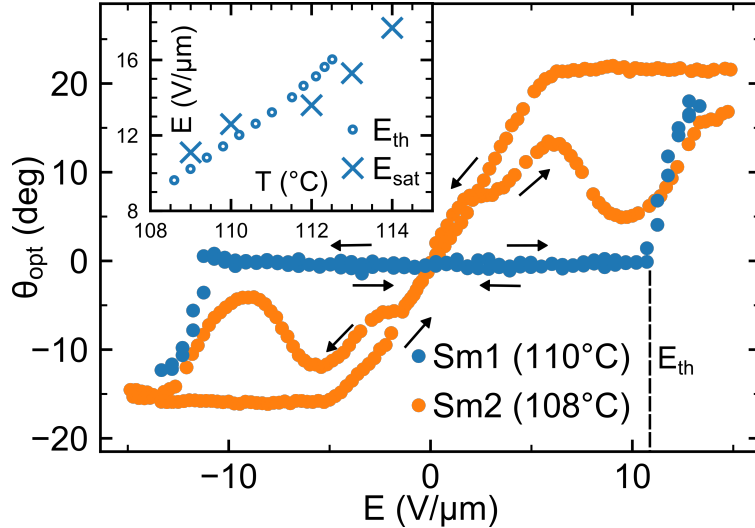


Figure 2.7: Optical tilt of PAL30 vs. applied field. The Sm1 phase shows no electrooptic response in weak fields $E < E_{\text{th}}$. Fields $E > E_{\text{th}}$ induce an electroclinic tilt and result in the formation of chiral domains. E_{th} , which becomes smaller with decreasing T (inset), matches closely E_{sat} , the field at which the induced polarization saturates, extracted from Figure 2.1(d). The Sm2 phase exhibits a chiral electroclinic effect near $E = 0$ and hysteresis in the field-induced helix unwinding to the $\text{SmC}_\text{S}P_\text{F}$ state.

In the lower part of the Sm1, and throughout the Sm2, Sm3 and Sm4 phases, the birefringence increases on application of an electric field, as seen in Figure 2.1(c), changing from yellow to orange. Measurements of Δn at $E = 0$ and $E = 20 \text{ V}/\mu\text{m}$ (Figures 2.1(c) and S6), show that the birefringences in the lower temperature phases with and without an applied field are of the order of $\Delta n_{\text{on}} \sim 0.12$ and $\Delta n_{\text{off}} \sim 0.10$. Assuming that the field-on $\text{SmC}_\text{S}P_\text{F}$ state (Figures 2.1(n–p) and S1) gives a uniform director orientation with the optic axis in the plane of the cell, then $\Delta n \sim 0.12$ would correspond to the maximal birefringence $n_3 - n_1$ of the $\text{SmC}_\text{S}P_\text{F}$ state. Modeling the bent-core molecule as two uniaxial, birefringent rods connected with an opening angle of Ψ , and tilting this molecule from z by an angle θ , we have calculated the birefringence of all of the states shown in Figure 2.1. If the Sm1 phase

is assumed to be a de Vries SmA, with azimuthally averaged molecules distributed on a tilt cone of angle θ , the best fit to the measured birefringence values Δn_{on} and Δn_{off} is obtained with $\Psi = 150^\circ$ and $\theta = 15^\circ$. The calculated birefringence as a function of temperature is shown in Figure S6.

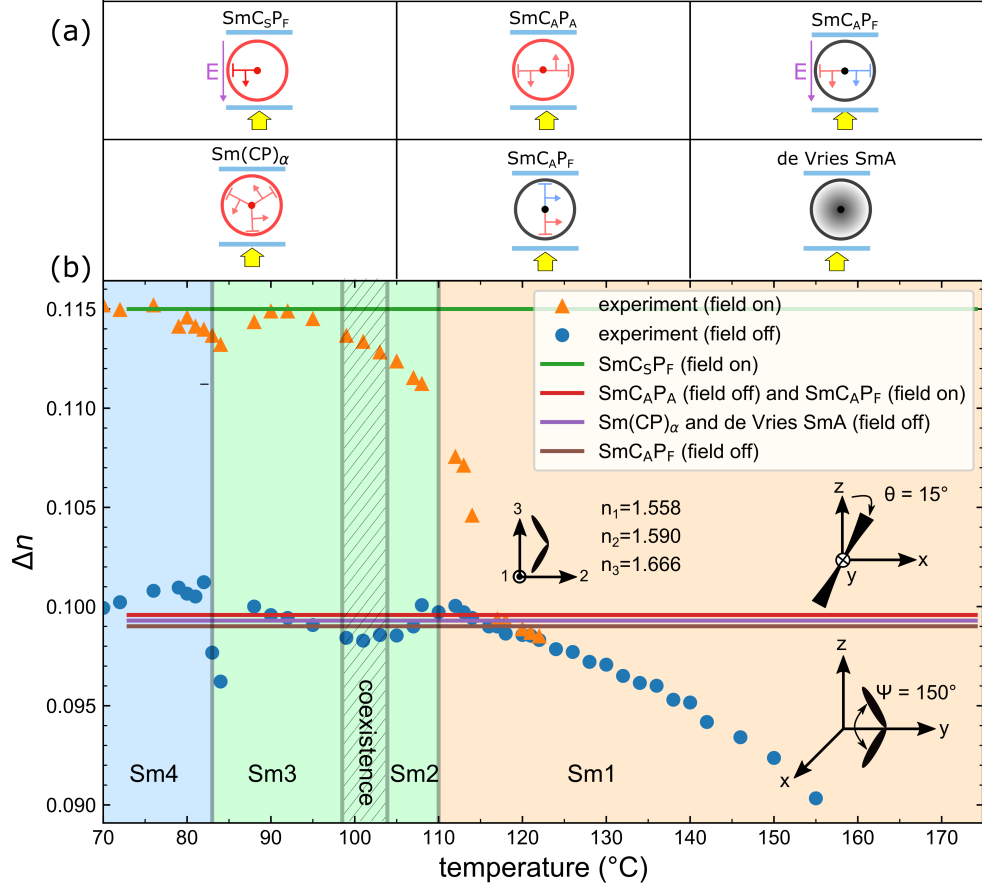


Figure 2.8: Calculated birefringence of PAL30, assuming Boulder phase assignments, shown as a function of temperature

The transitions between the smectic phases are difficult to see when $E = 0$ because they are all orthogonal in appearance, with an optic axis along z , and have similar birefringence. At the transition from Sm1 to the Sm2 phase, however, arbitrarily small electric fields induce molecular tilt in the (Figure 2.7), leading to the formation of optically distinct, conglomerate chiral domains with opposite tilt (Figures 2.1(h–j)), again corresponding to a field-induced transition to a *SmCsPF* state. The birefringence and orthogonal appearance of the Sm2

ground state are consistent with the helical superlayer structure indicated by RSoXS.

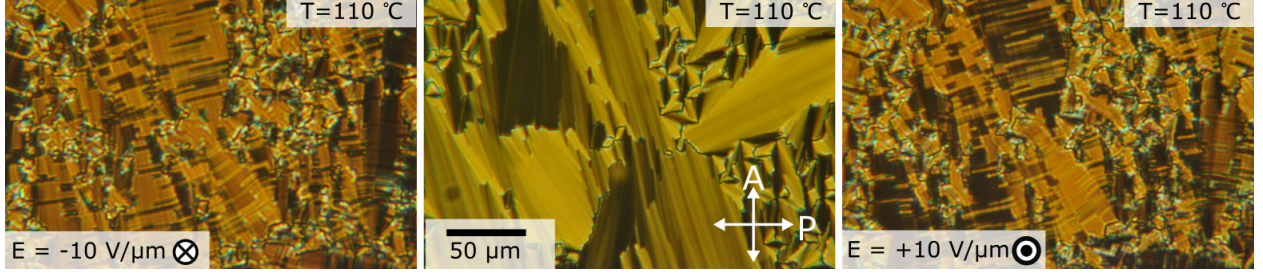


Figure 2.9: Textures of both the Sm2 ($\text{Sm}(\text{CP})_\alpha$) and Sm3 ($\text{SmC}_\text{A}\text{P}_\text{A}$) phases of PAL30: reminiscent of a $\text{SmC}_\text{A}\text{P}_\text{A}$ texture.

The texture and birefringence of the Sm3 phase in the absence of field are consistent with the $\text{SmC}_\text{A}\text{P}_\text{A}$ bilayer structure indicated by RSoXS. The field-induced conglomerate domain morphology in both the Sm2 and Sm3 phases is distinct from that of the undulating Sm1 tiger stripes, with straight domain boundaries that tend to form parallel to the layers, as in an antiferroelectric calamitic being driven to a ferroelectric state [20]. The optical tilt in these domains is found to be $\theta_{\text{opt}} \sim 18^\circ$.

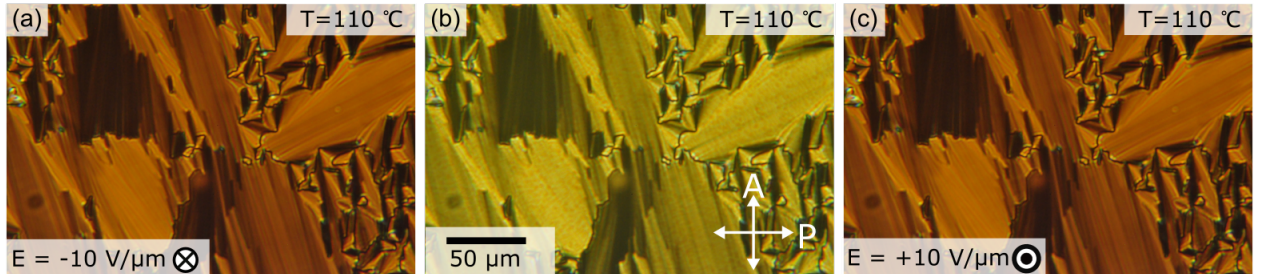


Figure 2.10: Textures of both the Sm2 ($\text{Sm}(\text{CP})_\alpha$) and Sm3 ($\text{SmC}_\text{A}\text{P}_\text{A}$) phases of PAL30: reminiscent of a $\text{SmC}_\text{A}\text{P}_\text{A}$ texture.

The response to applied field changes dramatically again at the transition from Sm3 to Sm4, with no visible brush rotation or evidence of domain formation at any E .

The birefringence in the Sm4 phase increases continuously with field, saturating at a value comparable to that observed in the field-induced Sm2 and Sm3 conglomerate domains.

2.1.5 Polarization Current

The polarization current, measured with a triangular applied field, for the entire phase sequence is shown vs. temperature in Figures 2.1(d) [Figure 2.11](#). The polarization current will be discussed in order of cooling.

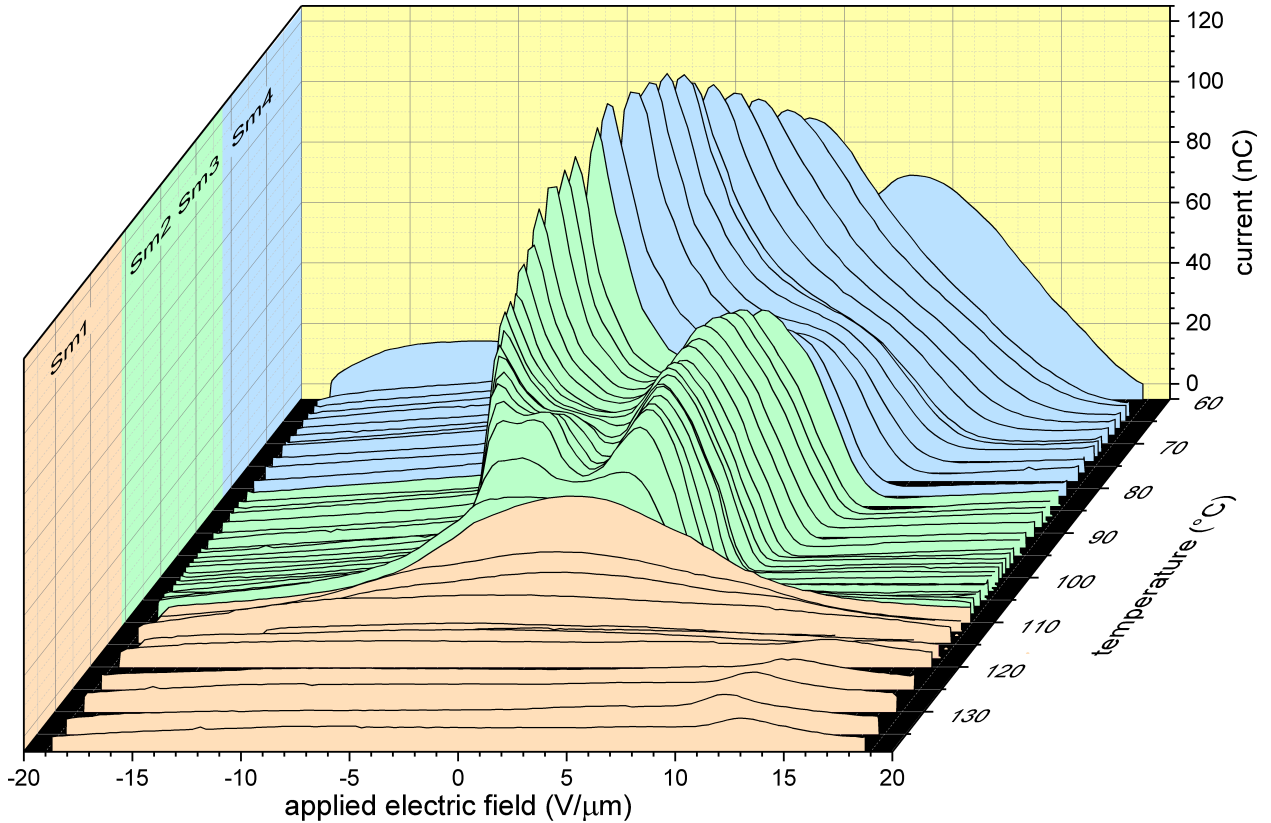


Figure 2.11: Polarization current of PAL30 shown as a function of the applied field strength.

Upon cooling from the isotropic, a single current bump centered about $E = 0$ first appears at lower temperatures in the Sm1 phase, indicating a Langevin-type field-induced orientation of \mathbf{P} , with a linear response near $E = 0$ and the current vanishing when \mathbf{P} becomes saturated (for $E \geq E_{\text{sat}}$).

Significantly, E_{sat} is similar in magnitude to E_{th} , the threshold field required for the Sm1 transition to chirality observed optically ([Figure 2.7](#), inset), indicating that the field first orders the Langevin system of initially azimuthally random molecular polarizations, with the

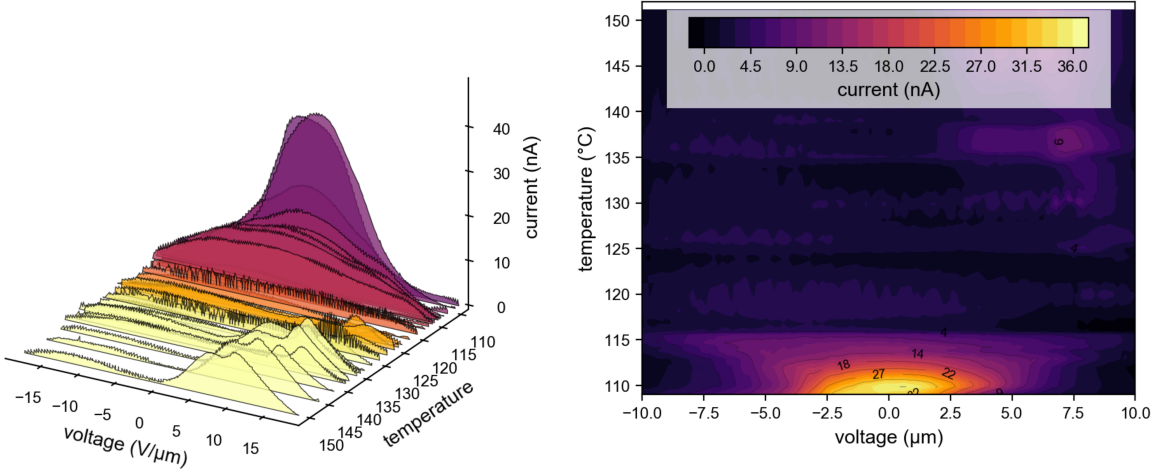


Figure 2.12: Zoomed in polarization current measurements for PAL30 in the high temperature Sm1 phase.

Sm1 remaining in an achiral state, and that the phase becomes chiral only at higher fields, once \mathbf{P} is saturated (Figure S10).

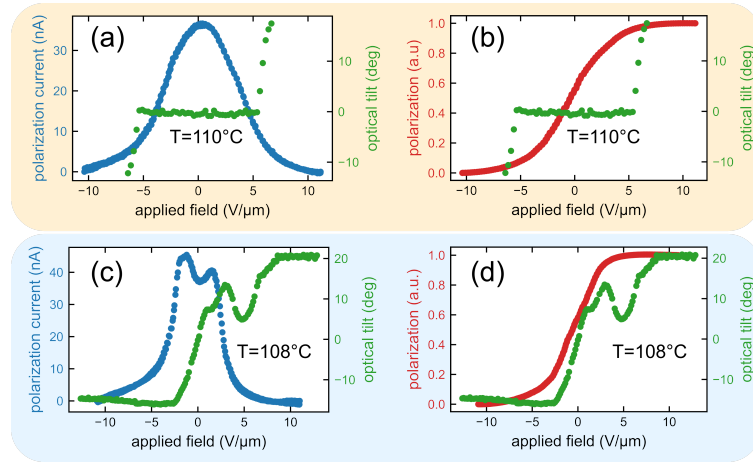


Figure 2.13: The polarization current and the optical tilt plotted as a function of applied field strength for both the Sm1 (de Vries SmA) (a,b) and the Sm2 ($\text{Sm}(\text{CP})_\alpha$) (c-d). The polarization current has additionally been integrated to calculate the time-dependant net polarization. The threshold electric field (E_{th}) required to manifest the tiger-stripes can be directly read from the green curve denoting the optical tilt (for $T=110^\circ\text{C}$, $E_{\text{th}} \approx 5 \text{ V}/\mu\text{m}$), and the saturation electric field where the net polarization is no longer changing (E_{sat}) can be directly read from the red curve, which denotes the net polarization, (for $T=110^\circ\text{C}$, $E_{\text{sat}} \approx 5 \text{ V}/\mu\text{m}$). Both E_{th} and E_{sat} are plotted in as the inset of Figure 2.7.

On cooling to the Sm2 phase, the polarization bump splits into three peaks roughly centered about $E = 0$ that evolve to two peaks on cooling through the Sm3, shown in Figure 2.14.

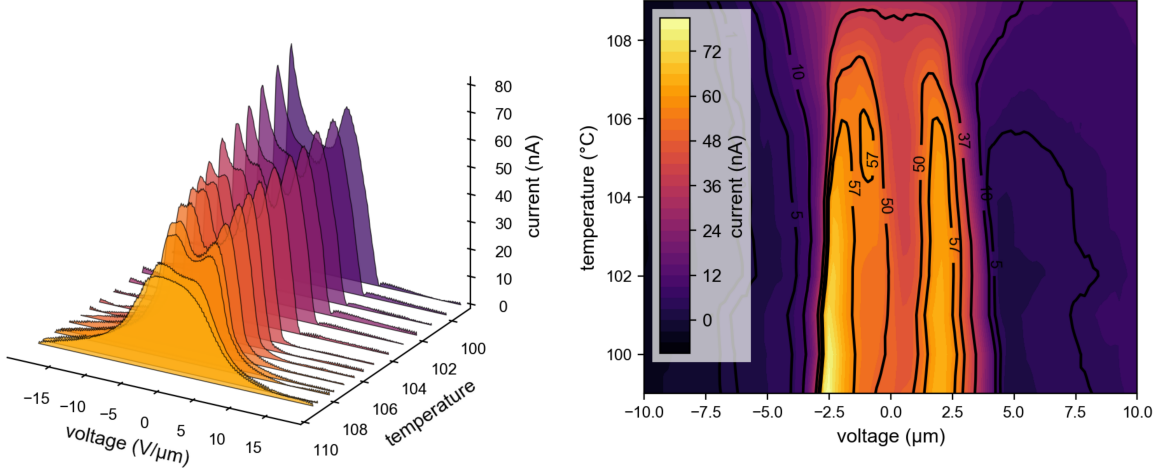


Figure 2.14: Polarization current of sm2 of PAL30 plotted against applied voltage

PAL30 thus transforms on cooling from the non-polar Langevin ground state of the Sm1, where $P = 0$ is enforced by entropy, to energetically stabilized ground states in which the spatial average of $\mathbf{P}(\mathbf{r})$ in the absence of applied field is also zero: the incommensurate helical winding of the polarization in the Sm2, and the antiferroelectric bilayer structure in the Sm3.

At the transition to the Sm4, a single current peak dominates, characteristic of the block polarization switching of a ferroelectric ground state that is surface-stabilized with \mathbf{P} parallel to the cell plates at $E = 0$, such as occurs in the orthorhombic SmAP_F phase [37].

The absence of brush rotation during the field-induced reorientation of the polarization in Sm4 is consistent with achiral $\text{SmC}_\text{A}P_\text{F}$ superlayer organization.

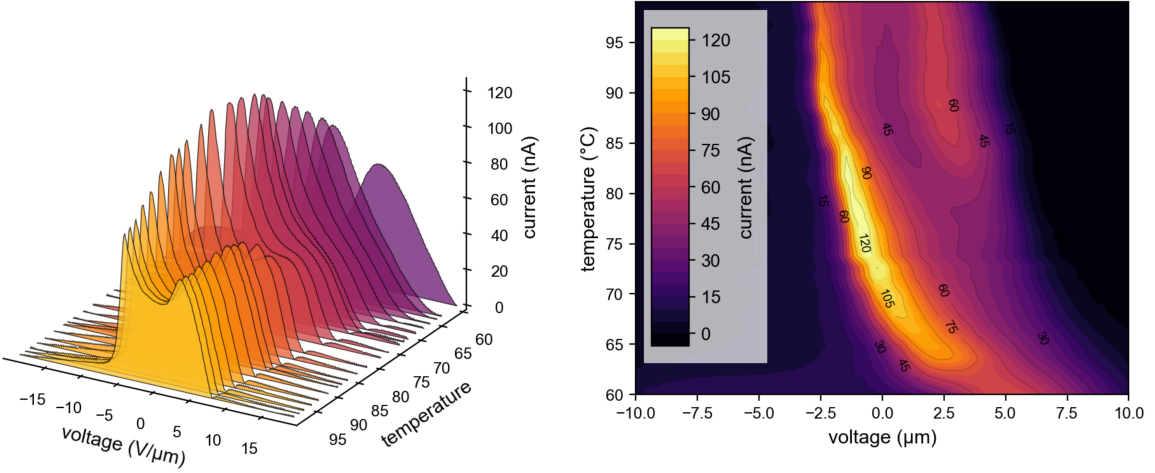
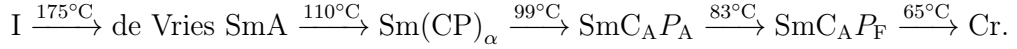


Figure 2.15: Polarization current measurements for PAL30 in the high temperature Sm1 phase.

2.2 Results and Discussion

In summary, X-ray and optical experiments show that PAL30, an achiral, bent-core mesogen, forms smectic liquid crystal phases with the molecules substantially tilted from the layer normal, with phase sequence:



The highest temperature phase exhibits short-ranged ordering of the tilt azimuth that is decoupled from the molecular polarization, forming a uniaxial, non-polar, achiral de Vries smectic A. An applied electric field of increasing magnitude continuously aligns the initially random polarization and the phase acquires orthorhombic symmetry. The field eventually saturates the polarization orientation, inducing a transition to a tilted, chiral, ferroelectric smectic state.

Upon cooling, a novel chiral, ferrielectric phase which we call the $\text{Sm}(\text{CP})_\alpha$ appears. This phase is similar to the SmC_α phase of chiral, rod-shaped molecules [24, 23, 14, 15], but with the chirality appearing here as a broken symmetry. A periodic azimuthal precession of the

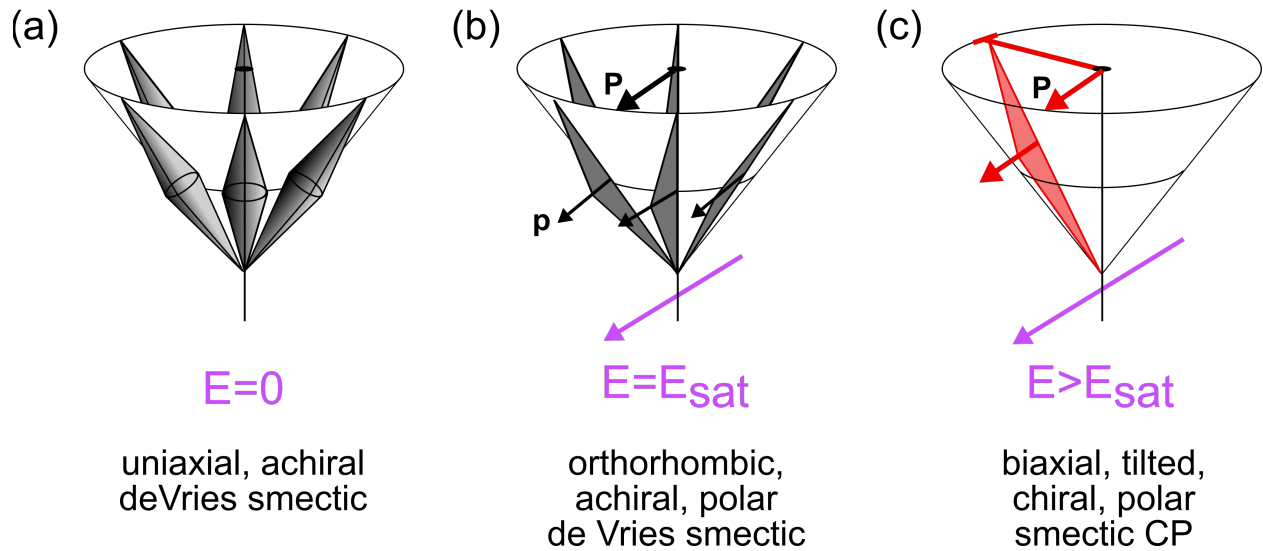


Figure 2.16: Evolution of de Vries SmA bent-core phase under the application of a field

director about the layer normal that is incommensurate with the smectic layering is confirmed by the presence of Bragg reflection peaks in carbon-edge resonant soft X-ray scattering. The absence of the corresponding resonant Umklapp peak unambiguously identifies this structure as a helical modulation of the orientational ordering in which molecules exhibit substantial coupled rotational/positional out-of-layer fluctuations, forming a twist-bend-like helix.

Chapter 3

Spontaneous Smectic Chirality Beyond the B2 Phase: A Homologous Series of Molecules related to PAL30

Now that the existance of the $\text{Sm}(\text{CP})_\alpha$ and $\text{SmC}_\text{A}P_\text{A}$ phase have been put on a firm footing, we can extend this study to a broad category of molecules that share the same core, but have variations in the tail length. Inspired by previous studies by the Dublin group[?, ?, ?]

add
vij's
new
paper

3.0.1 Textures of bent-core de Vries phase

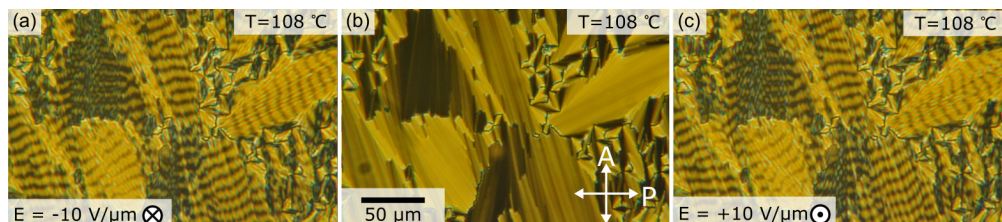


Figure 3.1:

3.0.2 Electro-optics of bent-core de Vries phase

text text

text

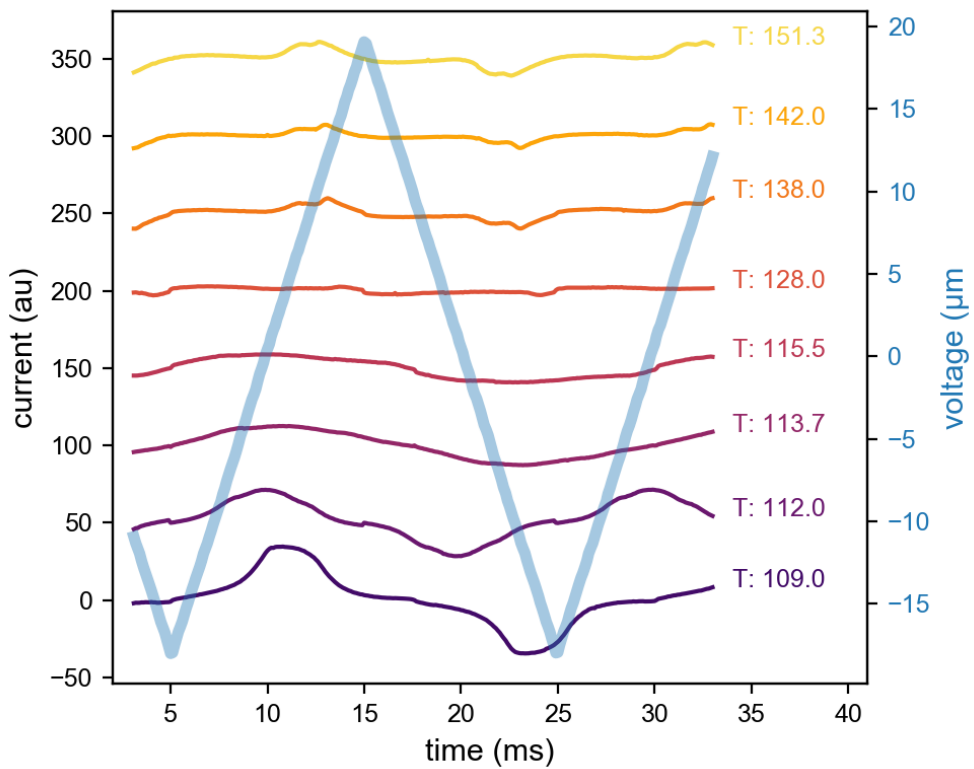


Figure 3.2:

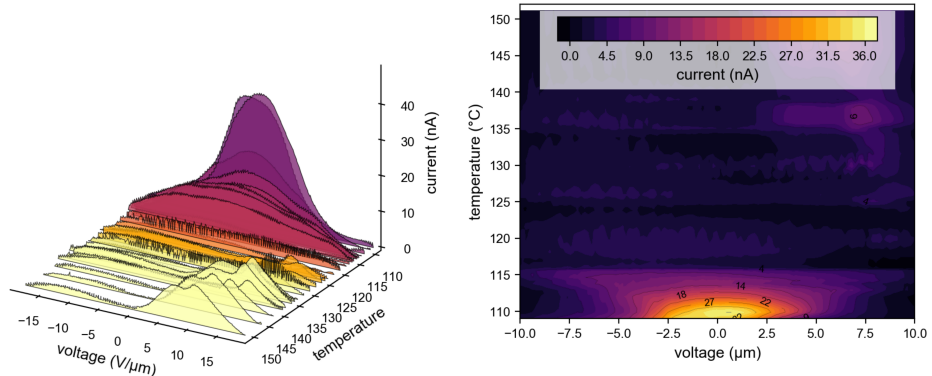


Figure 3.3:

3.0.3 X-ray analysis of bent-core de Vries phase

3.1 Discussion for the bent-core de Vries phase

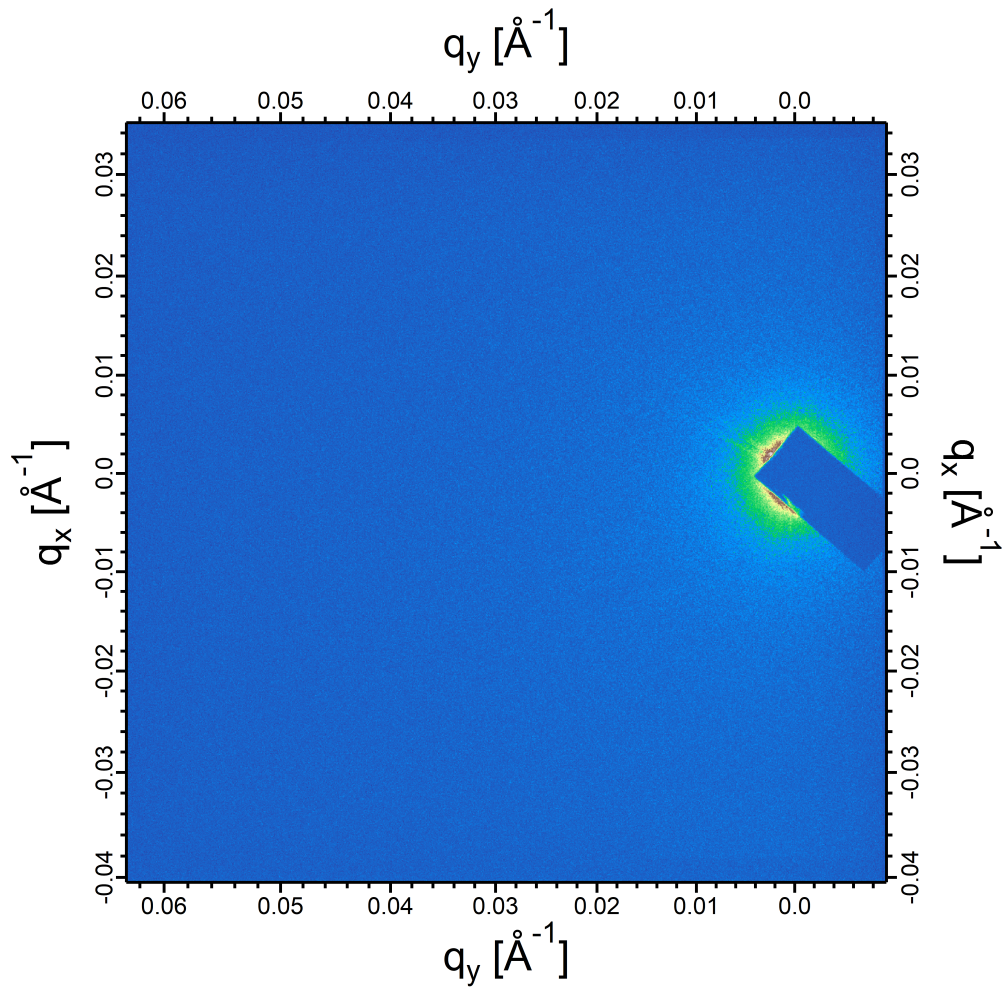


Figure 3.4:

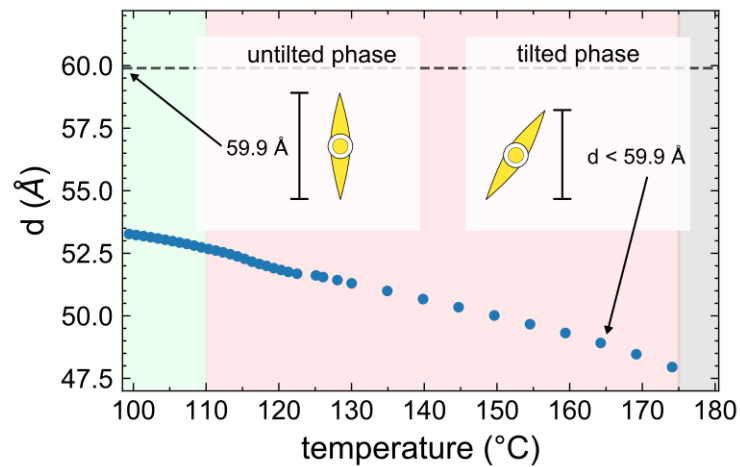


Figure 3.5:

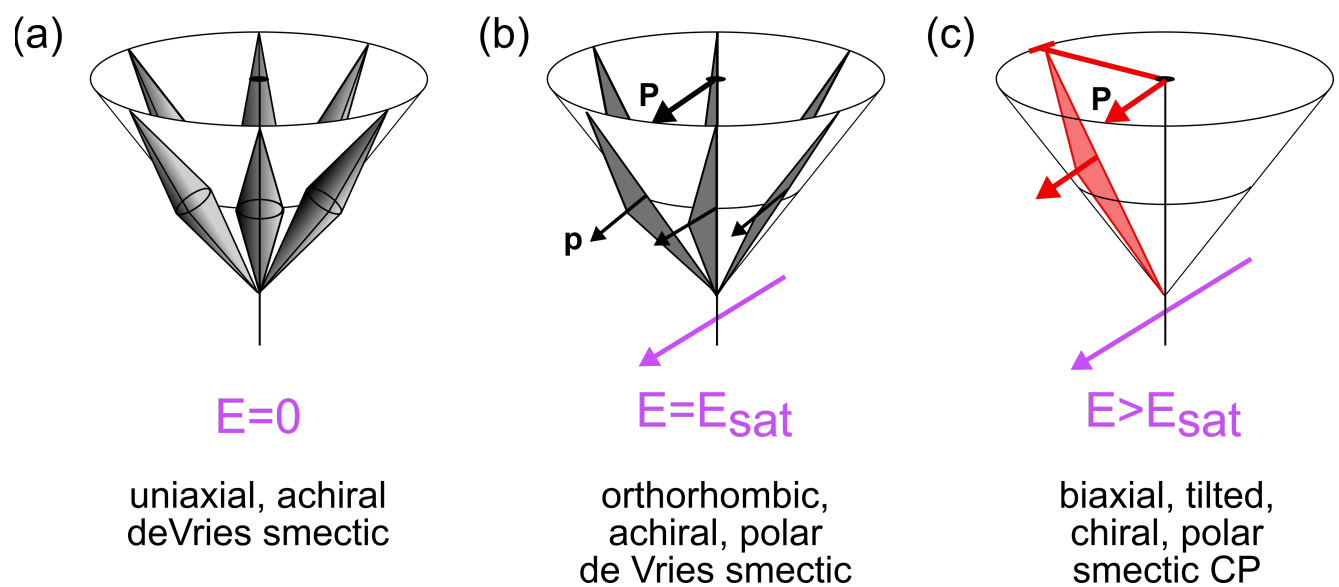


Figure 3.6:

Chapter 4

Metrology Applications of Fluid Crystals

4.1 Experimental Design

We created freely-suspended smectic films with racetrack geometry, as shown in Fig. 4.1, using 8CB (*4-n*-octylcyanobiphenyl), a fluid smectic A liquid crystal at room temperature that can be drawn into molecularly thin films freely suspended in air [47, 35, 29]. A mechanical drawing of the film holder is in the Supplemental Information.

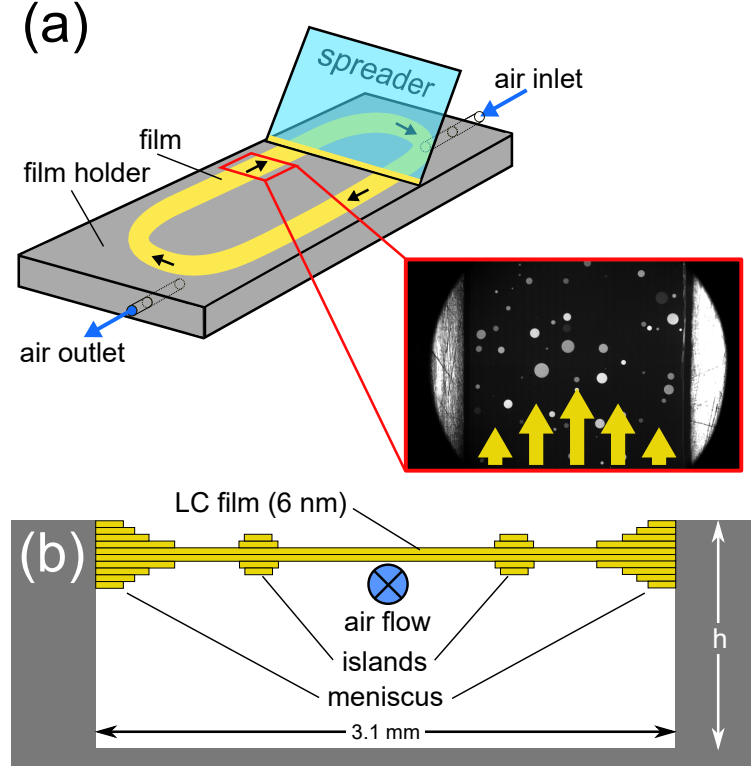


Figure 4.1: Smectic film flow meter geometry. (a) A stainless steel film holder ($45.2\text{ mm} \times 34.8\text{ mm} \times 7.6\text{ mm}$) has a $w = 3.1\text{ mm}$ -wide channel in the form of a racetrack cut to a depth $h = 3.7\text{ mm}$. At viewing ports centered along each ‘arm’, the channel is cut all the way through the film holder (a depth of 7.6 mm). Gas is coupled into and out of the system by means of co-linear, 2 mm -diameter holes at the ends of the film holder. Smectic films are created by coating the bottom of a glass coverslip (the spreader) with liquid crystal material and drawing it across the top opening of the channel. The film is shielded from random air currents from above by a sealed cover (not shown). The photomicrograph shows typical islands (localized regions with more layers than the background film) used to track flow of the film in one of the viewing regions of the racetrack. (b) Schematic cross-section of a smectic film suspended across the channel (not to scale). The film comprises an integer number of smectic layers and can be as thin as two molecules ($\sim 6\text{ nm}$). In general, a meniscus forms where the film contacts the edges of the channel.

Freely-suspended films are ideal flow sensors for several reasons. Because they are

so thin, they extract very little energy from the gas jet being measured. A comparison of the effective areal densities in our system assuming mass densities $\rho_{LC} = 1.008 \times 10^3 \text{ kg/m}^3$ and $\rho_{air} = 1.225 \text{ kg/m}^3$, and thicknesses 6 nm and 1 cm of the LC film and of the layer of air in the channel respectively, shows that the mass per unit area of the film is about 2000 times smaller than that of the air it is measuring, implying that smectic films should be very sensitive to the velocity of air flowing over them. Smectic films are intrinsically much more stable than films of conventional fluids, lasting up to several years in the laboratory, and have been used previously to probe 2D hydrodynamics [31, 18] and rheology [30], shear-stress measurements [27], and in pressure metrology [28, 46]. The application described here uses smectic films for flow measurements.

When a film is first drawn, it is typically only a few smectic layers thick and appears uniformly black in reflected light. In the prototype racetrack geometry sketched in Fig. 4.1(a), air is then injected at a known volumetric flow rate into the continuous rectangular channel located beneath the film. The inlet airflow is independently monitored using a mass airflow sensor (Honeywell AWM5101VN) capable of measuring flow rates between 0 and 5 standard litres per minute (SLPM). As the air flows through the channel, it shear couples to the liquid crystal, causing circulation of the film around the racetrack. This flow typically pulls some additional LC material in from the meniscus, leading to the formation of small, disc-like islands embedded in the film. Since the reflectance of thin, freely-suspended films depends quadratically on thickness[34], the islands are brighter than the background film and can easily be visualized using video microscopy. The motion of the islands is observed on the “backstretch” of the racetrack using a $5\times$ objective and captured using a high-speed video camera (Vision Research Phantom v12.1) at rates of 100–5000 frames per second. The islands are tracked using the open source Python library Trackpy [4], allowing us to use PTV methods [7, 2, 3, 32] to measure the velocity field of the film in the region of interest.

The device works by optically measuring the island velocity, which should be linearly coupled to the velocity of the airflow. In contrast to other mechanical flow meters, our flow

meter should thus be uniformly sensitive to airflow, regardless of the airflow velocity.

Our experimental approach has much in common with traditional PTV methods, where tracer particles are injected into the gas being measured and a light sheet created by a laser is used to define an illuminated plane, so that the tracer particles intersecting this plane can be tracked with a camera, mapping out the gas flow. A key difference is that our tracer particles (the islands) are embedded in a fluid with low vapor pressure ($< 10^{-6}$ torr)[?] that couples hydrodynamically to the gas flow, rather than relying on solid particles introduced into the gas. In the LC flow meter, the gas thus remains free of foreign tracer particles, making this a useful, non-invasive approach for systems where maintaining gas purity is important.

4.2 Theory and Simulation

In order to act as an ideal mechanical flow meter, the LC device should couple linearly to the gas flow (i.e., with a sensitivity independent of flow velocity) while having a minimal effect on the system being measured.

Linearity is an intrinsic feature of this system because of the standard no-slip boundary condition between two fluids in contact. Because the velocity of the air varies over the height of the channel, the average air and film velocities will be slightly different.

In order to model the behavior of the LC flow meter, we first consider two-phase, stratified flow in an infinitely long, rectangular pipe with symmetry about the midplane, a geometry that is amenable to an analytic approach [13, 16].

The symmetric rectangular pipe has the essential elements of the racetrack flow meter, a multiphase system where a thin fluid is surrounded by air, but has none of the complicating geometrical factors, allowing us to focus on the intrinsic properties of the air and film interaction. By varying the relative volume of the air and liquid phases (the phase fraction), we can estimate the effect of a fluid with the same thickness as a freely suspended film on the airflow.

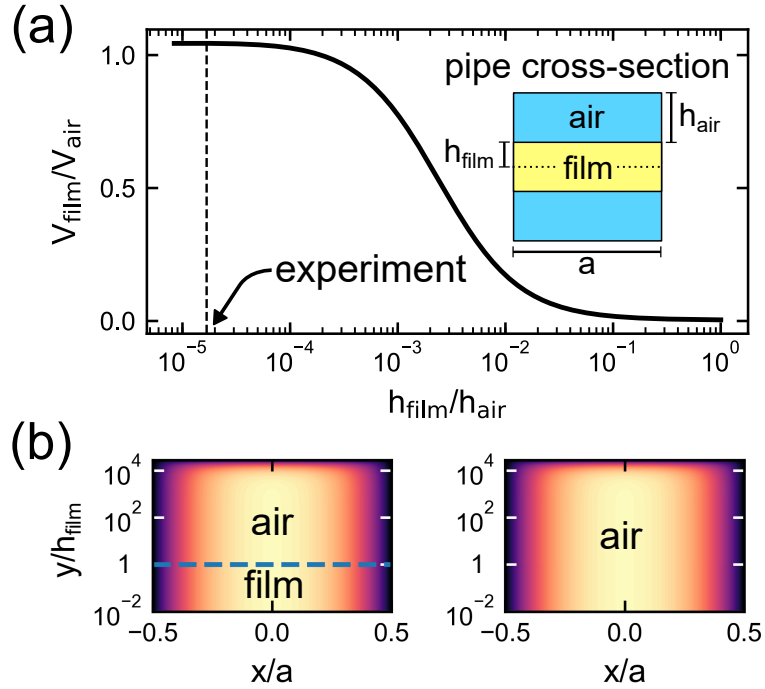


Figure 4.2: Analytic analysis of symmetric, two-phase, stratified fluid flow in an infinitely long pipe of width a . (a) Ratio between the average film and air velocities as a function of the phase fraction (the ratio of the volume of the fluid and the volume of the air, $\phi = h_{\text{film}}/h_{\text{air}}$). When the phase fraction is very small, the film is strongly coupled to the air and moves with the same speed. (b) Flow velocity in the top half of the pipe. At left, both air and film are flowing through the pipe (the blue dashed line demarcates the upper boundary of the film), while on the right only air is present. The y dimension is scaled by the half the thickness of the LC film, h_{film} . The flow fields in these two cases are practically indistinguishable, suggesting that the influence of the LC film on the airflow is negligible.

We solved the Navier-Stokes equations to determine the airflow in the pipe both with and without the LC film, using appropriate viscosities for the air (1.8×10^{-5} Pa s) and LC film (5.2×10^{-2} Pa s)[?]. At values of the phase fraction corresponding to the experiment (with a thick LC film of 60 molecular layers, $\phi \sim 10^{-5}$), the flow of the LC film is found to be coupled identically to that of the air (Fig. 4.2(a)). Furthermore, the air flow in the presence of the LC film is essentially indistinguishable from the flow in the absence of the film (Fig. 4.2(b)), suggesting that, at least in this idealized geometry, the film extracts a negligible amount of energy from the air flow. Details of these calculations are given in the Supplemental Information.

We numerically modeled the flow of air in the 3D racetrack geometry, without the liquid crystal film but choosing track dimensions and flow parameters consistent with our experiments.

Modeling the air flow alone allows us to see the “natural state” of flow in the racetrack geometry in the absence of the LC film. As the results of the analytical modeling in the previous section suggest that the film has a negligible influence on the airflow, we expect these airflow-only simulations to closely mimic the experimental behaviour.

The results of these simulations then allow us to see whether the geometry of the racetrack modifies the linear sensitivity predicted from the analytical model. We can also test the assumption that the film has a negligible impact on the overall flow behaviour by comparing the results of the air-flow simulations to the observed experimental flow behaviour.

The simulations were performed using OpenFOAM, an open-source fluid dynamics solver that uses a SIMPLE algorithm[45]. The results are summarized in Fig. 4.3 with further details given in the Supplemental Information. The simulations indicate that at low inlet velocity values ($\lesssim 0.55$ m/s) the air stream in the channel splits, so that it flows in the same absolute direction along both arms of the racetrack. At $v_{\text{in}} = 0.55$ m/s, the airflow is predicted to transition to homogeneous, clockwise circulation.

The net force on an LC film in contact with the air stream is the sum of the shear forces along the entire length of the racetrack, for which there are two main contributions: the air moving along the shortest distance from the inlet to the outlet (at speed v_2), and the air moving along the other side of the racetrack (at speed v_1). Because the LC film is incompressible, if v_1 and v_2 are in the same absolute direction, as in Fig. 4.3(a), then the steady state film velocity is $v_{\text{film}} \propto v_2 - v_1$. This predicted film speed is in general lower than but roughly proportional to the inlet air flow, as shown in Fig. 4.3(b).

We think that the chaotic flow we observe in the racetrack is a manifestation of the ‘split-flow’ predicted by the simulations. We hypothesize that the film acts to bias the air-film system to a circulating regime, explaining why the air-film onset to circulating flow happens

at lower inlet velocities than the simulations predict for pure airflow.

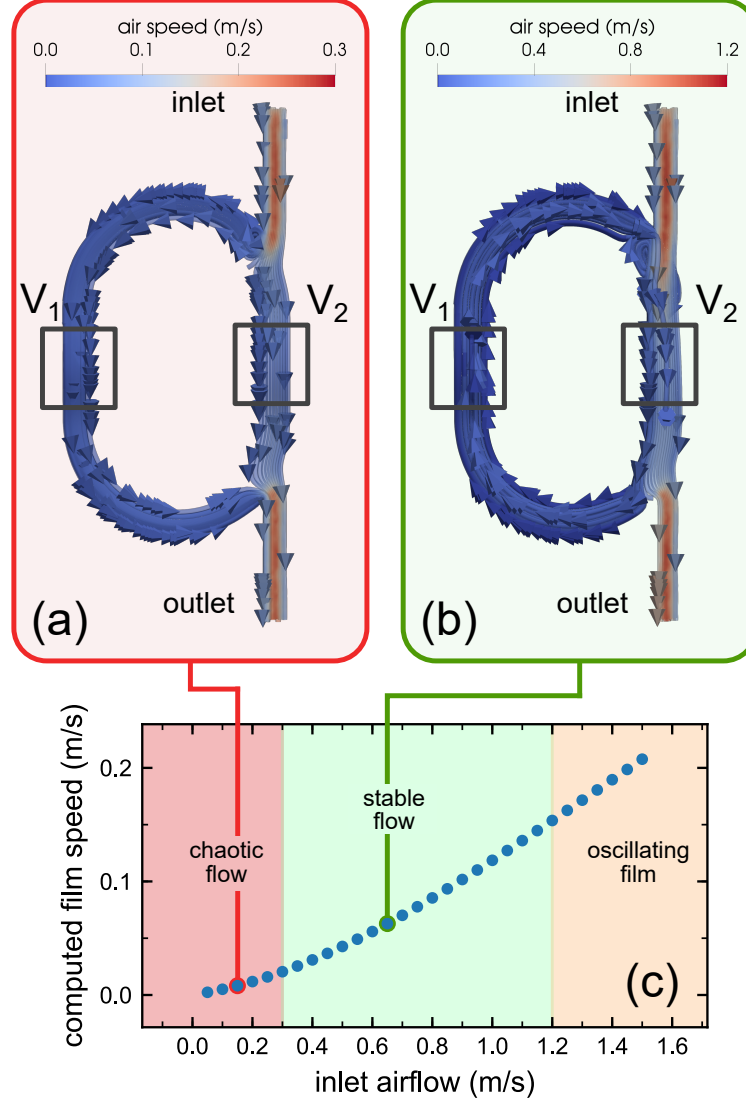


Figure 4.3: Computed airflow in the racetrack geometry. (a) Model velocity field for inlet velocity $v_{\text{inlet}} = 0.15 \text{ m/s}$. The air does not circulate uniformly in the same sense around the racetrack, instead splitting between the front and back legs. (b) Model velocity field for inlet velocity $v_{\text{inlet}} = 0.65 \text{ m/s}$. Above a transition inlet velocity of $v_{\text{inlet}} = 0.55 \text{ m/s}$, the air circulates uniformly around the racetrack. (c) Predicted net film speed ($v_{\text{film}} \propto v_2 - v_1$) for a range of inlet velocities. The slope of this curve gives an average theoretical sensitivity of $S = 0.15$. The background shading reflects the experimental observations with different inlet velocities: for $v_{\text{in}} < 0.3 \text{ m/s}$, the film flow is chaotic; for $0.3 \text{ m/s} < v_{\text{in}} < 1.2 \text{ m/s}$, the film exhibits stable Poiseuille flow; for $v_{\text{in}} > 1.2 \text{ m/s}$, the film undergoes rapid out-of-plane oscillations that make particle tracking impractical.

In summary, the analytic and numerical models both suggest that freely-suspended LC

films in racetrack geometry should make excellent flow detectors, linearly coupling to and stabilizing the air flow.

4.3 Results and Discussion

We measured the velocity fields of LC films coupled to inlet airflows in the range 0.1 SLPM–0.4 SLPM. We observed three main regimes of film flow behaviour, indicated by the shading in Fig. 4.3(c). Below a threshold inlet air velocity ($v_{\text{in}} < 0.3 \text{ m/s}$), the flow is characterized by time-dependent, chaotic behavior, with flow reversal and eddy currents observed in the films. This behavior is likely due to flow splitting of the type shown in Fig. 4.3(a), where the incoming air stream is divided between the short and long arms of the racetrack.

At intermediate air inlet velocities ($0.3 \text{ m/s} < v_{\text{in}} < 1.2 \text{ m/s}$), the film undergoes uniform, counter-clockwise circulation around the racetrack, as shown in Fig. 4.4(a), with a Poiseuille flow profile across the film that stabilizes in less than 1 second. The observed threshold speed for the transition from chaotic flow to uniform circulation ($v_{\text{in}} \sim 0.3 \text{ m/s}$) is somewhat lower than predicted by the simulations for airflow alone ($v_{\text{in}} \sim 0.55 \text{ m/s}$). This suggests that the film acts to stabilize homogeneous flow, promoting a uniform, regular circulation of the film and air. Because our measurement relies on obtaining regular, simple flow, the stable regime is clearly optimal for operation of the flow meter, and extending the usable range to lower inlet velocities is a clear advantage of the LC film-air system. At high air inlet velocities ($v_{\text{in}} > 1.2 \text{ m/s}$), the film oscillates rapidly up and down, causing the islands to go in and out of focus and the film eventually to break.

A comparison of the spatially averaged film speed measured half way along the back stretch of the racetrack to the independently measured inlet airflow is plotted in Fig. 4.4(b). The average slope of this graph gives a measured sensitivity of the flow meter of $S = 0.09$. This is slightly less than the sensitivity predicted from the pure airflow simulations, a difference

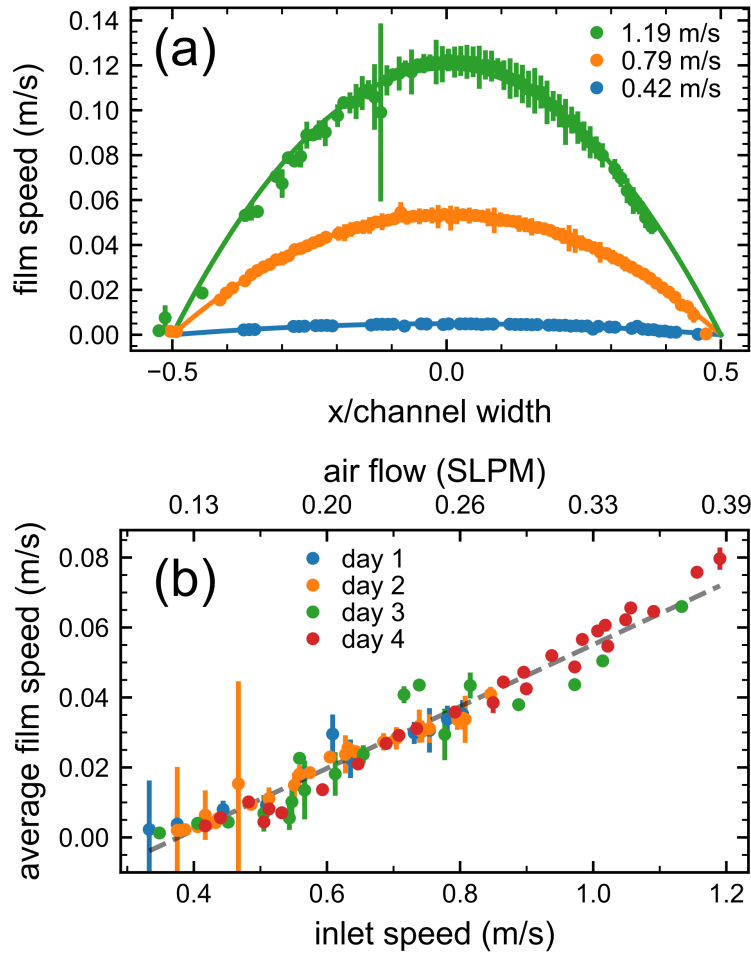


Figure 4.4: Characterization of flow meter. (a) Velocity profiles over the width of the racetrack channel, with each point corresponding to a specific tracked island. The profiles are well described by parabolas (smooth curves), confirming Poiseuille flow over a wide-range of inlet velocities. At higher velocities, the data are noisier due to the relatively paucity of islands that can be captured in sequential frames. The left-right asymmetry in the number of measurements is an artifact due to defects on one side of the camera sensor. (b) Spatially averaged film velocity in the observation region as a function of inlet air velocity. Measurements were performed over four separate days, using more than 30 films. The volumetric flow rate of the air being injected into the racetrack through the inlet was measured using an independent mechanical sensor. The average film speed is linearly proportional to the speed of the air at the device inlet, with a sensitivity that is independent of flow rate.

which we attribute to air loss during the air-injection process. With some refinement of the racetrack geometry, we would expect to extend the accessible measurement range to lower velocities. The upper velocity limit could be raised by implementing measures to equalize the air pressure across the film. We believe that such differences in air pressure are responsible for the rapid vertical oscillations observed at high flow rates.

By harnessing the unique properties of freely-suspended smectic films, we have demonstrated a method for mechanical measurement of air flow that has intrinsically linear sensitivity. This technique could usefully be applied to mapping the velocity field of gases flowing through exotic microfluidic geometries in two dimensions.

Bibliography

- [1] Jordan P. Abberley, Ross Killah, Rebecca Walker, John M. D. Storey, Corrie T. Imrie, Miroslaw Salamonczyk, Chenhui Zhu, Ewa Gorecka, and Damian Pociecha. Heliconical smectic phases formed by achiral molecules. *Nature Communications*, 9:2856, JUL 17 2018.
- [2] A. A. Adamczyk and L. Rimal. 2-Dimensional particle tracking velocimetry (PTV): Technique and image processing algorithms. 6(6):373–380.
- [3] Ronald J. Adrian and Jerry Westerweel. *Particle Image Velocimetry*. Cambridge University Press.
- [4] Daniel B. Allan, Thomas Caswell, Nathan C. Keim, and Casper M. van der Wel. Trackpy: Trackpy v0.4.1.
- [5] P. Barois, H. Gleeson, C. C. Huang, and R. Pindak. Application of x-ray resonant diffraction to structural studies of liquid crystals. *The European Physical Journal Special Topics*, 208(1):333–350, Jun 2012.
- [6] Nattaporn Chattham, Eva Korblova, Renfan Shao, David M. Walba, Joseph E. Macلنnan, and Noel A. Clark. Triclinic Fluid Order. *Phys. Rev. Lett.*, 104(6):067801, February 2010.
- [7] Th. Dracos. Particle Tracking Velocimetry (PTV). In Th. Dracos, editor, *Three-Dimensional Velocity and Vorticity Measuring and Image Analysis Techniques: Lecture Notes from the Short Course Held in Zürich, Switzerland, 3–6 September 1996*, ERCOFTAC Series, pages 155–160. Springer Netherlands.
- [8] A. Eremin and A. Jákli. Polar bent-shape liq. cryst. ÅS from molecular bend to layer splay and chirality. *Soft Matter*, 9(3):615–637, 2013.
- [9] Alexey Eremin, Stephan Stern, and Ralf Stannarius. Electrically induced tilt in achiral bent-core liquid crystals. *Phys. Rev. Lett.*, 101:247802, Dec 2008.
- [10] Sonja Findeisen-Tandel, Martin W Schröder, Gerhard Pelzl, Uta Baumeister, Wolfgang Weissflog, S Stern, Alexandru Nemes, Ralf Stannarius, and Alexey Eremin. Multistage polar switching in bent-core mesogens. *The European Physical Journal E*, 25(4):395–402, 2008.

- [11] CL Folcia, J Ortega, J Etxebarria, S Rodriguez-Conde, G Sanz-Enguita, K Geese, C Tschierske, V Ponsinet, P Barois, R Pindak, et al. Spontaneous and field-induced mesomorphism of a silyl-terminated bent-core liquid crystal as determined from second-harmonic generation and resonant x-ray scattering. *Soft Matter*, 10(1):196–205, 2014.
- [12] Helen F. Gleeson and Linda S. Hirst. Resonant X-ray Scattering: A Tool for Structure Elucidation in Liquid Crystals. *ChemPhysChem*, 7(2):321–328, February 2006.
- [13] George Wheeler Govier and Khalid Aziz. *The Flow of Complex Mixtures in Pipes*. Society of Petroleum Engineers, 2 edition.
- [14] L. S. Hirst, S. J. Watson, H. F. Gleeson, P. Cluzeau, P. Barois, R. Pindak, J. Pitney, A. Cady, P. M. Johnson, C. C. Huang, A-M. Levelut, G. Srajer, J. Pollmann, W. Caliebe, A. Seed, M. R. Herbert, J. W. Goodby, and M. Hird. Interlayer structures of the chiral smectic liquid crystal phases revealed by resonant x-ray scattering. *Phys. Rev. E*, 65:041705, Apr 2002.
- [15] C. C Huang, Shun Wang, LiDong Pan, Z. Q Liu, B. K McCoy, Yuji Sasaki, Kenji Ema, P Barois, and Ron Pindak. Liquid crystal mesophases beyond commensurate four-layer periodicity. *Liq. Crys. Rev.*, 3(1):58–78, 2015.
- [16] Dongeun Huh, Yi-Chung Tung, Hsien-Hung Wei, James B. Grotberg, Steven J. Skerlos, Katsuo Kurabayashi, and Shuichi Takayama. Use of Air-Liquid Two-Phase Flow in Hydrophobic Microfluidic Channels for Disposable Flow Cytometers. *4(2):141–149*.
- [17] Jan Ilavsky. Nika: Software for two-dimensional data reduction. *J. Appl. Crystallogr.*, 45(2):324–328, 2012.
- [18] Tatiana Kuriabova, Thomas R. Powers, Zhiyuan Qi, Aaron Goldfain, Cheol Soo Park, Matthew A. Glaser, Joseph E. MacLennan, and Noel A. Clark. Hydrodynamic interactions in freely suspended liquid crystal films. *94(5):052701*.
- [19] Anne-Marie Levelut and Brigitte Pansu. Tensorial x-ray structure factor in smectic liquid crystals. *Phys. Rev. E*, 60(6):6803, 1999.
- [20] Jian-Feng Li, Xin-Yi Wang, Erik Kangas, P. L. Taylor, Charles Rosenblatt, Yoshi-Ichi Suzuki, and P. E. Cladis. Reversible propagating fingers in an antiferroelectric liquid crystal. *Physical Review B*, 52(18):R13075, 1995.
- [21] Darren R. Link, Giorgio Natale, Renfan Shao, Joseph E. MacLennan, Noel A. Clark, Eva Körblova, and David M. Walba. Spontaneous Formation of Macroscopic Chiral Domains in a Fluid Smectic Phase of Achiral Molecules. *Science*, 278(5345):1924–1927, December 1997.
- [22] Feng Liu, Michael A Brady, and Cheng Wang. Resonant soft x-ray scattering for polymer materials. *Eur. Polym. J.*, 81:555–568, 2016.

- [23] P. Mach, R. Pindak, A.-M. Levelut, P. Barois, H. T. Nguyen, H. Baltes, M. Hird, K. Toyne, A. Seed, J. W. Goodby, C. C. Huang, and L. Furenlid. Structures of chiral smectic-C mesophases revealed by polarization-analyzed resonant x-ray scattering. *Phys. Rev. E*, 60(6):6793–6802, December 1999.
- [24] P. Mach, R. Pindak, A.-M. Levelut, P. Barois, H. T. Nguyen, C. C. Huang, and L. Furenlid. Structural characterization of various chiral smectic-C phases by resonant X-ray scattering. *Phys. Rev. Lett.*, 81(5):1015, 1998.
- [25] T. Niori, T. Sekine, J. Watanabe, T. Furukawa, and H. Takezoe. Distinct ferroelectric smectic liq. cryst. consisting of banana shaped achiral molecules. *J. Mater. Chem.*, 6(7):1231–1233, January 1996.
- [26] Y. P. Panarin, M. Nagaraj, S. Sreenilayam, J. K. Vij, A. Lehmann, and C. Tschierske. Sequence of four orthogonal smectic phases in an achiral bent-core liquid crystal: Evidence for the smap_α phase. *Phys. Rev. Lett.*, 107(24):247801, December 2011.
- [27] D. S. Parmar. A novel boundary layer sensor utilizing domain switching in ferroelectric liquid crystals. 62(2):474–479.
- [28] Devendra S. Parmar and Harlan K. Holmes. Pressure sensor using liquid crystals.
- [29] Ronald Pindak and David Moncton. Two-dimensional systems. 35(5):57.
- [30] Zhiyuan Qi, Kyle Ferguson, Yancey Sechrest, Tobin Munsat, Cheol Soo Park, Matthew A. Glaser, Joseph E. MacLennan, Noel A. Clark, Tatiana Kuriabova, and Thomas R. Powers. Active microrheology of smectic membranes. 95(2):022702.
- [31] Zhiyuan Qi, Zoom Hoang Nguyen, Cheol Soo Park, Matthew A. Glaser, Joseph E. MacLennan, Noel A. Clark, Tatiana Kuriabova, and Thomas R. Powers. Mutual Diffusion of Inclusions in Freely Suspended Smectic Liquid Crystal Films. 113(12):128304.
- [32] Markus Raffel, Christian E. Willert, Fulvio Scarano, Christian J. Kähler, Steve T. Wereley, and Jürgen Kompenhans. *Particle Image Velocimetry: A Practical Guide*. Springer.
- [33] R. Amaranatha Reddy, Chenhui Zhu, Renfan Shao, Eva Korblova, Tao Gong, Yongqiang Shen, Edgardo Garcia, Matthew A. Glaser, Joseph E. MacLennan, David M. Walba, and Noel A. Clark. Spontaneous Ferroelectric Order in a Bent-Core Smectic Liquid Crystal of Fluid Orthorhombic Layers. *Science*, 332(6025):72–77, April 2011.
- [34] Charles Rosenblatt and Nabil M. Amer. Optical determination of smectic A layer spacing in freely suspended thin films. 36(6):432–434.
- [35] Charles Rosenblatt, Ronald Pindak, Noel A. Clark, and Robert B. Meyer. Freely Suspended Ferroelectric Liquid-Crystal Films: Absolute Measurements of Polarization, Elastic Constants, and Viscosities. 42(18):1220–1223.

- [36] Mirosław Salamończyk, Nataša Vaupotič, Damian Pociecha, Cheng Wang, Chenhui Zhu, and Ewa Gorecka. Structure of nanoscale-pitch helical phases: blue phase and twist-bend nematic phase resolved by resonant soft x-ray scattering. *Soft matter*, 13(38):6694–6699, 2017.
- [37] Yongqiang Shen, Tao Gong, Renfan Shao, Eva Korblova, Joseph E MacLennan, David M Walba, and Noel A Clark. Effective conductivity due to continuous polarization reorientation in fluid ferroelectrics. *Phys. Rev. E*, 84(2):020701, 2011.
- [38] S. Sreenilayam, M. Nagaraj, Y. P. Panarin, J. K. Vij, A. Lehmann, and C. Tschierske. Properties of Non-Tilted Bent-Core Orthogonal Smectic Liquid Crystal. *Mol. Cryst. Liq. Cryst.*, 553(1):140–146, January 2012.
- [39] Sithara P. Sreenilayam, Yuri P. Panarin, Jagdish K. Vij, Vitaly P. Panov, Anne Lehmann, Marco Poppe, Marko Prehm, and Carsten Tschierske. Spontaneous helix formation in non-chiral bent-core liq. cryst. with fast linear electro-optic effect. *Nat. Commun.*, 7:11369, May 2016.
- [40] Yoichi Takanishi, Youko Ohtsuka, Yumiko Takahashi, Sungmin Kang, and Atsuo Iida. Chiral doping effect in the b2 phase of a bent-core liquid crystal: The observation of resonant x-ray satellite peaks assigned to the 5/10 layer periodic structure. *Europhysics Letters*, 109(5):56003, 2015.
- [41] H. Takezoe and Y. Takanishi. Bent-Core Liquid Crystals: Their Mysterious and Attractive World. *Jpn. J. Appl. Phys.*, 45(2R):597, February 2006.
- [42] Hideo Takezoe and Alexey Eremin. *Bent-shaped Liquid Crystals: Structures and Physical Properties*. CRC Press, 2017.
- [43] Hideo Takezoe, Ewa Gorecka, and Mojca Čepič. Antiferroelectric liquid crystals: interplay of simplicity and complexity. *Rev. Mod. Phys.*, 82(1):897, 2010.
- [44] Cheng Wang, Dong Hyun Lee, Alexander Hexemer, Myung Im Kim, Wei Zhao, Hirokazu Hasegawa, Harald Ade, and Thomas P Russell. Defining the nanostructured morphology of triblock copolymers using resonant soft x-ray scattering. *Nano Lett.*, 11(9):3906–3911, 2011.
- [45] H. G. Weller, G. Tabor, H. Jasak, and C. Fureby. A tensorial approach to computational continuum mechanics using object-oriented techniques. *12(6):620–631*.
- [46] S. V. Yablonskii, K. Nakano, A. S. Mikhailov, M. Ozaki, and K. Yoshino. Pressure sensor based on freely suspended ferroelectric liquid crystal film. *80(4):571–573*.
- [47] Charles Y. Young, Ronald Pindak, Noel A. Clark, and Robert B. Meyer. Light-Scattering Study of Two-Dimensional Molecular-Orientation Fluctuations in a Freely Suspended Ferroelectric Liquid-Crystal Film. *40(12):773–776*.

- [48] Fan Zhang, Jan Ilavsky, Gabrielle G Long, John P. G Quintana, Andrew J Allen, and Pete R Jemian. Glassy carbon as an absolute intensity calibration standard for small-angle scattering. *Metall. Mater. Trans. A*, 41(5):1151–1158, 2010.
- [49] Chenhui Zhu, Michael R Tuchband, Anthony Young, Min Shuai, Alyssa Scarbrough, David M Walba, Joseph E MacLennan, Cheng Wang, Alexander Hexemer, and Noel A Clark. Resonant carbon k-edge soft x-ray scattering from lattice-free heliconical molecular ordering: soft dilative elasticity of the twist-bend liquid crystal phase. *Phys. Rev. Lett.*, 116(14):147803, 2016.
- [50] Chenhui Zhu, Cheng Wang, Anthony Young, Feng Liu, Ilja Gunkel, Dong Chen, David Walba, Joseph MacLennan, Noel Clark, and Alexander Hexemer. Probing and controlling liquid crystal helical nanofilaments. *Nano Lett.*, 15(5):3420–3424, 2015.